1990   Thesis/Dissertation

A Two-Dimensional Balanced Model of Internal Frontogenesis
in Geostrophic and Isentropic Coordinates

Norman H. Mandy

AFIT Student at: Colorado State University

AFIT/CI/CIA - 90-081

AFIT/CI
Wright-Patterson AFB OH 45433

DTIC
ELECTE
OCT 23 1990
S   D
B

69

UNCLASSIFIED

THESIS

A TWO-DIMENSIONAL BALANCED MODEL OF INTERNAL FRONTOGENESIS
IN GEOSTROPHIC AND ISENTROPIC COORDINATES

Submitted by

Norman H. Mandy

Department of Atmospheric Science

In partial fulfillment of the requirements

for the degree of Master of Science

Colorado State University

Fort Collins, Colorado

Spring 1990

90 10 20 089

COLORADO STATE UNIVERSITY

March 29, 1990

WE HEREBY RECOMMEND THAT THE THESIS PREPARED UNDER OUR SUPERVISION BY NORMAN H. MANDY ENTITLED A TWO-DIMENSIONAL BALANCED MODEL OF INTERNAL FRONTOGENESIS IN GEOSTROPHIC AND ISENTROPIC COORDINATES BE ACCEPTED AS FULFILLING IN PART REQUIREMENTS FOR THE DEGREE OF MASTER OF SCIENCE.

Committee on Graduate Work

_____

_____

_____

_____

_____
Adviser

_____
Department Head

ii

ABSTRACT OF THESIS

A TWO-DIMENSIONAL BALANCED MODEL OF INTERNAL FRONTOGENESIS IN GEOSTROPHIC AND ISENTROPIC COORDINATES

Here we seek to both improve and simplify the method by which upper frontogenesis may be studied. Using a two-dimensional form of the geostrophic momentum approximation in geostrophic/isentropic coordinates, our dynamic model reduces to a predictive equation for the potential pseudo-density (inverse Rossby-Ertel potential vorticity), with associated diagnostic equation for the Bernoulli function from which the wind and mass fields can be calculated. Ageostrophic motions are implicit, and vertical motions retained for the adiabatic case employed, by this choice of coordinates. Initialization of the domain incorporates a realistic vertical distribution of the mass field along with upper/lower boundaries which are either isobaric/isentropic or constant potential vorticity surfaces. Vertical wind shears such as are commonly associated with baroclinic waves are idealized and act as the forcing mechanism for frontogenesis.

Major model results include the formation of upper fronts with associated wind and thermal fields which, when viewed together, are well correlated with observations of these parameters in terms of magnitude and gradient as well as their proximity to one another. Well-defined folding of the dynamic tropopause occurs in geostrophic space; thus, unlike previous balanced models, the transformation back to physical space is not required in order to produce the desired results. However, we show that performing the coordinate transformation enhances the realism of the results.

Our findings document the applicability of the geostrophic momentum approximation to non-curved flows containing high relative vorticity, and the simplicity of the dynamics

when applied to these particular coordinates. Further, we find that generalizing the forcing mechanism can also produce noteworthy aspects of internal frontogenesis; this was accomplished by extracting an essential feature of baroclinic waves—vertical wind shearing—and incorporating it first into the classical deformation field and later applying it to the zonal flow directly. The results suggest more can be learned about frontogenesis by application of balanced two-dimensional theory even when relatively extreme simplifications, such as adiabatic, frictionless flow, are made.

Norman H. Mandy
Department of Atmospheric Science
Colorado State University
Fort Collins, Colorado 80523
Spring 1990

Accession For	
NTIS GRA&I	☑
DTIC TAB	☐
Unannounced	☐
Justification	
By	
Distribution/	
Availability Codes	
Dist	Avail and/or Special
A-1	

ACKNOWLEDGEMENTS

CONTENTS

LIST OF FIGURES

Chapter 1

INTRODUCTION

The study of internal (upper-level) fronts has been an active field of research since the late 1920s, when upper-air instruments first became operational. Some of the salient structures of these fronts—features such as static stability in the frontal layer, transverse horizontal temperature gradients, and the nearly isothermal layer in the region now referred to as the tropopause and lower stratosphere—were observed early on. The prominent interpretation which grew out of these observations was that of the Bergen School—a continuous frontal theory—which evolved into a "deep" polar frontal model where fronts were thought to extend from the surface to the tropopause. Not surprisingly, both the avenues and roadblocks to knowledge of upper-level fronts have paralleled the advance of the instrumentation necessary to measure their characteristics; for example, the Bergen School theory fell into disuse, at least initially, primarily due to the lack of supporting observational evidence.

One important advance, advocated by Reed and Danielson (1959), was that fronts were no longer viewed as regions separating polar from tropical tropospheric air. In this model, upper fronts are perceived as a secondary phenomenon of a tropopause folding event through tilting effects, and that these fronts may be defined as separating tropospheric and stratospheric air instead of separating two distinct tropospheric air masses. Two implications of this model are that we can specifically account for stratospheric-tropospheric mass exchange, a result which was later confirmed (e.g. Briggs et al., 1963), and that upper fronts may form independently of surface fronts. Observational studies by Shapiro et al. (1987) indicate the upper low pressure vortex and jet stream associated with a folding tropopause occur in arctic weather systems as well as the more commonly referred

to mid-latitude and subtropical systems. This data led to their proposal of a new model for the meridional structure of the tropopause and primary wind systems—referred to as a three-fold model—wherein there exists stratospheric-tropospheric exchange through these folds accompanied by subtropical, polar, and arctic jetstreams, respectively.

Tropopause folding as a mechanism for upper frontogenesis is not inconsistent with the modern view, which considers such frontogenesis to be related to the development of baroclinic waves. Kinematically, however, baroclinic waves with their associated wind shear patterns result in a complex process wherein differential advection of both the thermal and wind fields tends to hinder attempts at understanding any single aspect of the problem. One way to gain information about these processes is to make idealizations in such a way as to reproduce frontal characteristics which are consistent with those observed as growing out of the baroclinic wave. For example, we can isolate frontogenesis by idealizing the wind and thermal fields in ways known to lead to frontogenesis; such an approach is used in the work of Hoskins (1971) and Hoskins and Bretherton (1972) where a geostrophic deformation field acts on a weak initial temperature gradient. This procedure produces realistic scale contraction wherein the fluid concentrates into narrow zones, resulting in cross-frontal gradients which are about an order of magnitude greater than those along the front. Hoskins (1974) has shown that similar results are obtained for the steady state problem as well, and that frontogenesis increases for this case when the thermal wind opposes the basic flow.

Although the Primitive Equations (PEs) have been the primary tool for integrations used in numerical weather prediction, they have the disadvantage of being so general as to preclude significant analytical manipulations. In particular, the lack of balance conditions implies the desired fields (e.g. wind and mass) cannot be obtained by a simple invertibility relationship. On the other hand, the relatively extreme simplification of the PEs resulting in the Quasi-geostrophic (QG) approximation cannot mathematically handle the dynamics which occur, among other areas, in and near a midlatitude front. Fortunately, the study of fronts benefits from the application of another more modern tool described below which has been successfully applied to, for example, ageostrophic secondary frontal flows by Hoskins and Draghici (1977) and the balanced squall line model of Schubert *et al.* (1989).

The Geostrophic Momentum Approximation (first alluded to by Eliassen, 1948, and hereafter referred to as GMA) represents a compromise between the complex accuracy of the PEs and the simplicity of QG theory. The GMA equations, a filtered set in that they cannot describe gravity wave propagation, are more general than the QG equations since fewer terms are dropped from the PEs. In fact, they bear more formal resemblance to the PEs than they do to those resulting from QG theory: advection is by the total wind and vertical advection is retained in the momentum equation. Perhaps most importantly, though, the essential properties of a three dimensional vorticity equation, conservation of potential vorticity, and the energy equation are all formally consistent with those derived from the PEs. Additionally, the GMA is valid for flows where the vertical component of relative vorticity is on the order of the coriolis parameter—an important consideration for the study of fronts, jets, and many other observable atmospheric phenomena. It should be noted here, however, that the GMA is not valid in regions where the flow is highly curved (defined as any region where the curvature vorticity is on the order of the shear vorticity) and it is not clear what if any effects are neglected due to this assumption.

Ideally, we would like to retain the benefits of a general theory such as the GMA, while retaining as many analytical and numerical benefits as possible arising from the relative simplicity of QG theory. Hoskins (1975) and Hoskins and Draghici (1977) made progress toward such a theory by advocating a coordinate transformation which, when applied to the GMA, were termed the "Semigeostrophic" (SG) equations. With these new horizontal coordinates, the advecting velocities become geostrophic as in the QG equations. However, because the new equations are mathematically identical to the GMA, we conclude the ageostrophic advections are retained implicitly in the coordinate transformation. Similarly, newly defined ageostrophic components allow retention of both a continuity equation and vector momentum equation which are formally identical to QG theory, but with the latter equation retaining vertical motion which is again implicit in the change of coordinates. The thermodynamic equation becomes more general since its vertical motion is against the (geostrophic) potential vorticity, which varies in three dimensional space, instead of being against the static stability parameter, which varies only in the vertical.

Further development of SG theory was made by Schubert *et al.* (1987, 1989) with the simultaneous use of geostrophic and isentropic coordinates, which allows the system of equations to be reduced to a predictive equation for the potential pseudo-density (inverse Rossby-Ertel potential vorticity) and a diagnostic relationship for the Bernoulli function. With this choice of coordinates, the ageostrophic circulation becomes entirely implicit as well. Of course, for adiabatic motions the total θ-derivative disappears, and the potential density becomes a conservative quantity. The potential density equation has only one component with θ as the vertical coordinate since, as noted by Haynes and McIntyre (1987) for the PEs and later applied to the GMA equations by Schubert *et al.* (1989), there is no net transport of potential vorticity across any isentrope; thus, potential vorticity can be neither created nor destroyed in a layer bounded by two isentropes. The application to the GMA equations of the impermeability of isentropes to potential vorticity is one of several indications of the consistency of the GMA.

There are other benefits gained by utilization of the SG equations. For example, because the Jacobian of the coordinate transformation is also the dimensionless vertical component of absolute vorticity, resolution of a numerical scheme is enhanced in geostrophic space in regions of a relative maximum of this quantity (in such regions, the shift obtained by transforming a field back to physical space is the greatest). Thus, for a given grid spacing, features which may be unresolveable in physical space are captured in geostrophic space and shifted back to physical space. This procedure often produces realistic replications (e.g. vorticity patterns near a cold front produced by Hoskins and West, 1979).

So far we have considered from a historical perspective some of the conditions under which upper fronts may form, and discussed the relevance of certain tools and approaches to the study of the frontogenesis process. The approach of Hoskins mentioned earlier has aspects which preface the possibility of further research. Keyser and Pecnick (1985) allude to these possibilities by pointing out that the primary success of two-dimensional semigeostrophic theory in the context of frontogenesis has thus far been with regard to surface fronts. They proceed to develop a PE model which simultaneously includes the effects of confluence (horizontal deformation) and horizontal shear, along with three- dimensional characteristics, resulting in the best representations of upper fronts to date in a

two-dimensional model; still, there is the lingering question of whether a balanced model can successfully model internal frontogenesis in two dimensions or, as stated by Buzzi *et al.* (1981) with regard to semigeostrophic theory, a three dimensional representation is required.

Figure 1.1 shows a model-produced upper front which apparently is as realistic a result as has been achieved for two-dimensional balanced flows to date. Notice the front doesn't extend deep into the troposphere, and the slight folding of the dynamic tropopause is achieved only by the use of the geostrophic coordinate in the model. This should be compared with figure 1.2, which is representative of the growing base of observational data on tropopause folding events. As is frequently the case, the fronts in this figure formed within a developing mid-latitude cyclone, with a fold on either side of the upper trough in the height field. Here we see the formation of deep fronts with well-defined folds, strong jet streaks, and sharply sloping isentropes in the vicinity of the fronts.

Thus we attempt to both simplify and improve on previous results regarding the frontogenesis process. Specifically, we address the following questions: (1) Can the model equations be simplified and generalized by using both geostrophic and isentropic coordinates? (2) Will the simultaneous inclusion of (a) a continuous potential vorticity field in the vertical and (b) a height-dependent deformation field, which has not been attempted within the context of semigeostrophic theory, result in a more realistic depiction of the upper-level frontogenesis process?

In order to answer these questions, we use the f-plane system of equations with the GMA and proceed in Chapter 2 to develop the three dimensional potential density equation and associated invertibility relation in geostrophic coordinates. This system is closed by simply including the geostrophic and hydrostatic relations which, already, is a simplification of the system in its various "physical" coordinate forms. In Chapter 3, the reduction of this model to two dimensions in the transformed cross-frontal plane allows an analytic solution of the prediction equation and a de-coupling of the predictive and diagnostic equations from a numerical standpoint. Frontogenesis is idealized following the general approach of Hoskins *et al.* (1971, 1972) and Buzzi *et al.* (1981), but with the
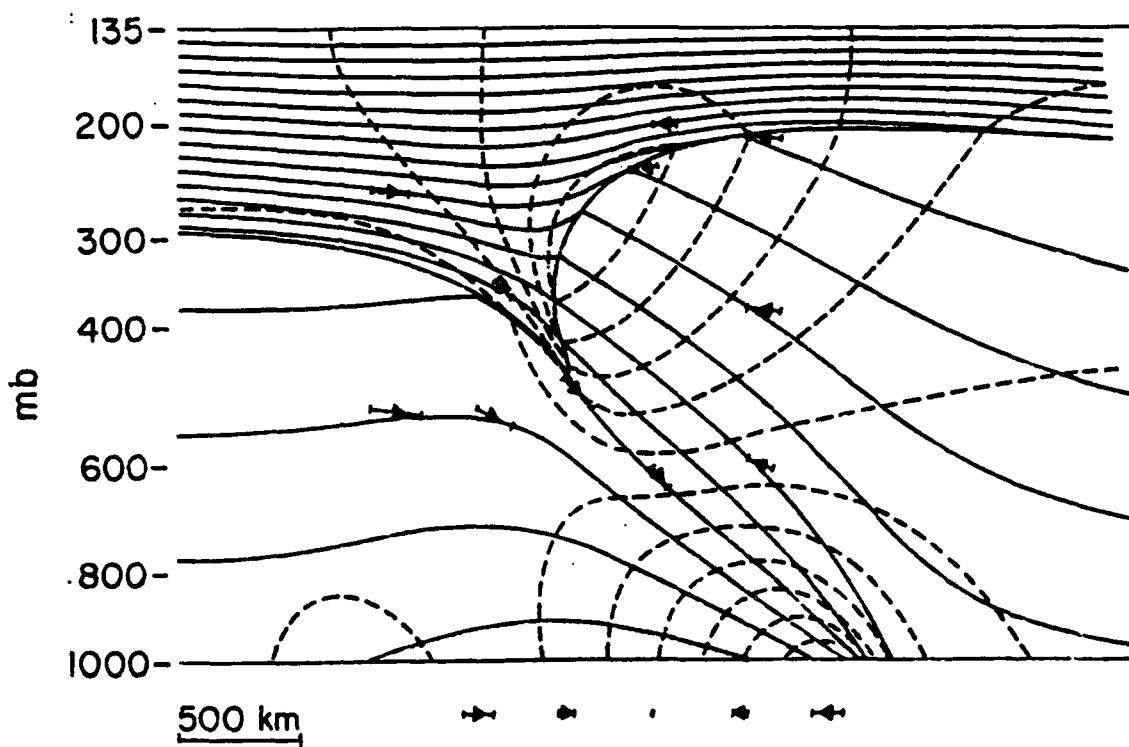
Figure 1.1: A two-dimensional balanced model result showing formation of a folded tropopause or constant potential vorticity surface (shown as the heavy solid line) and associated upper-front, using a deformation field as the forcing mechanism and the geostrophic horizontal coordinate. Thin solid lines are isentropes, and isotachs are dashed. Taken from Hoskins (1972).
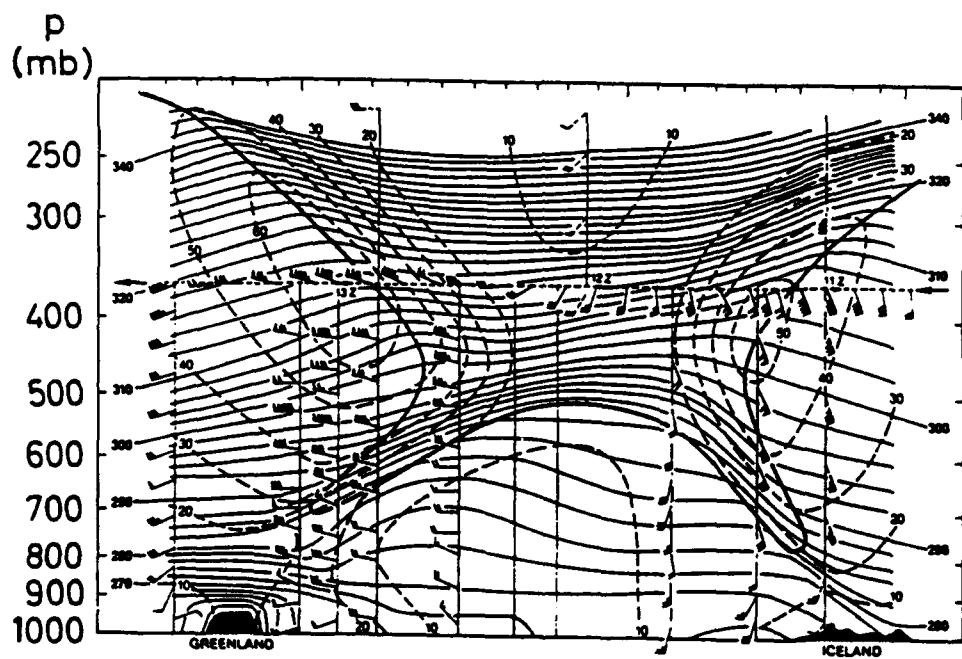
Figure 1.2: Cross-section through an Islandic Low as observed on 12 April 1983. The tropopause shown is a constant potential vorticity surface and is represented by the heavy solid line separating stratospheric air (clear) and tropospheric air (shaded). Thin solid lines and dashed lines are as in figure 1.1, also. Taken from Shapiro (1985).

aforementioned additions: a generalized height dependent deformation rate, and a more realistic initialization of the potential vorticity field. The upper and lower boundaries are chosen as isentropic as well as isobaric surfaces. The resulting equations are shown to take the same form as those for the specific case where the deformation rate is constant. The use of a two dimensional model has the historical advantage of producing realistic transverse secondary circulations and, in addition, with our choice of coordinates we show the simplicity with which these circulations can be recaptured.

Results show the combination of allowing the rate of deformation to vary vertically and prescribing the initial field of potential vorticity as a continuous one do indeed produce realistic upper level fronts, perhaps most notably a true folding of the dynamic tropopause which in some cases extends deep into the troposphere. In these cases the tropopause is defined as a constant potential vorticity surface (see Danielsen, 1980). Although at this point it was unclear what aspect(s) of our model produced realistic frontal parameters, we felt the key ingredient was the vertical wind shear characteristic of the deformation field. Thus an additional question was whether a generalization of the wind field, wherein assumed vertical shears are consistent with baroclinic wave development, would produce similar results. Further model runs in Chapter 4 verify this hypothesis with respect to formation of upper fronts. In this case we also redefined the initial state in a manner known to isolate formation of internal fronts; thus, results of Chapter 4 verify that realistic modeling of upper frontal parameters can be accomplished when disassociated from surface fronts.

Chapter 2 reviews the three-dimensional theory from which our model is derived. Chapter 3 defines the two-dimensional model, describes results of selected model runs, and compares these results with previous work. In Chapter 4 further testing and comparison is done by redefining the initial field. A summary follows in Chapter 5.

Chapter 2

THEORY REVIEW

2.1 Review of the Potential Density Equation

We begin with the f-plane system of equations with the geostrophic momentum approximation (Eliassen, 1948; Hoskins, 1975). Proceeding with an analysis similar to that of Schubert *et al.* (1989), we will arrive at a simple predictive equation for the potential pseudo-density (inverse Rossby-Ertel potential vorticity). Later, in our two dimensional model, this predictive equation will take on an even simpler form. Assuming the flow is frictionless, and using potential temperature as the vertical coordinate, our system becomes

$$\frac{Du_g}{Dt} - fv + \frac{\partial M}{\partial x} = 0, \tag{2.1}$$

$$\frac{Dv_g}{Dt} + fu + \frac{\partial M}{\partial y} = 0, \tag{2.2}$$

$$\frac{\partial M}{\partial \theta} = \Pi, \tag{2.3}$$

$$\frac{D\sigma}{Dt} + \sigma \left(\frac{\partial u}{\partial x} + \frac{\partial v}{\partial y} + \frac{\partial \dot{\theta}}{\partial \theta} \right) = 0 \tag{2.4}$$

where $(u_g, v_g) = f^{-1}(-\partial M/\partial y, \partial M/\partial x)$ are the components of geostrophic velocity, (u, v) the horizontal components of the total velocity, $\Pi = c_p (p/p_0)^\kappa$ the Exner function, $M = \theta\Pi + \phi$ the Montgomery potential, $\sigma = -\partial p/\partial \theta$ the pseudo-density, $\dot{\theta} = D\theta/Dt$ the vertical theta velocity, and

$$\frac{D}{Dt} = \frac{\partial}{\partial t} + u\frac{\partial}{\partial x} + v\frac{\partial}{\partial y} + \dot{\theta}\frac{\partial}{\partial \theta} \tag{2.5}$$

the total derivative. The vertical component of the vorticity equation can be derived from (2.1) and (2.2) and takes the form

$$\frac{D\zeta}{Dt} + \zeta \left(\frac{\partial u}{\partial x} + \frac{\partial v}{\partial y} + \frac{\partial \dot{\theta}}{\partial \theta} \right) - \left(\xi\frac{\partial}{\partial x} + \eta\frac{\partial}{\partial y} + \zeta\frac{\partial}{\partial \theta} \right) \dot{\theta} = 0, \tag{2.6}$$

where the components of the absolute vorticity vector are given by

$$\xi = f\frac{\partial(X,Y)}{\partial(y,\theta)}, \qquad \eta = f\frac{\partial(X,Y)}{\partial(\theta,x)}, \qquad \zeta = f\frac{\partial(X,Y)}{\partial(x,y)}, \qquad (2.7)$$

and X and Y are defined below in (2.10). We can eliminate the divergence between (2.4) and (2.6) to obtain one form of the potential density equation:

$$\frac{D\sigma^*}{Dt} + \frac{\sigma^*}{\zeta}\left(\xi\frac{\partial}{\partial x} + \eta\frac{\partial}{\partial y} + \zeta\frac{\partial}{\partial\theta}\right)\dot\theta = 0, \qquad (2.8)$$

where

$$\sigma^* = \frac{f}{\zeta}\sigma \qquad (2.9)$$

is the potential pseudo-density, or potential density (PD) for short. With θ as the vertical coordinate we can simplify our system of equations (hence, the vorticity and pseudo-density equations also) significantly for motions which are adiabatic. We will make the adiabatic assumption later in chapter 3 when we develop the (dry) frontal model.

2.2   Review of Semigeostrophic Theory

2.2.1   Coordinate Transformation

Since (2.8) involves advection by the total wind, this equation along with the invertibility relation we formulate in section 2.2.2 will not form a closed system. Expressed in physical space, then, this system would not be appropriate for modeling purposes unless we were to solve an additional equation. With this as the initial motivation, we now introduce the geostrophic coordinates, where in this case we simultaneously use the isentropic vertical coordinate approach following the arguments of Schubert *et al.* (1989). The horizontal transformation has the affect of switching the function of physical and geostrophic coordinates, respectively, by making geostrophic variables independent variables and the physical variables dependent variables. We define geostrophic coordinates in the usual way:

$$(X,Y,\Theta,T) = (x + v_g/f, y - u_g/f, \theta, t), \qquad (2.10)$$

where the term "geostrophic" is a result of the fact that, for the frictionless case described in our governing equations, $DX/Dt = u_g$ and $DY/Dt = v_g$, as can be easily seen from

(2.1), (2.2), and (2.10). Thus, a particle following the motion in geostrophic space moves with the geostrophic wind.

The relationships between derivatives in (x, y, θ) and (X, Y, Θ) space are written as

$$\frac{\partial}{\partial t} = \frac{\partial X}{\partial t}\frac{\partial}{\partial X} + \frac{\partial Y}{\partial t}\frac{\partial}{\partial Y} + \frac{\partial}{\partial T}, \tag{2.11}$$

$$\frac{\partial}{\partial x} = \frac{\partial X}{\partial x}\frac{\partial}{\partial X} + \frac{\partial Y}{\partial x}\frac{\partial}{\partial Y}, \tag{2.12}$$

$$\frac{\partial}{\partial y} = \frac{\partial X}{\partial y}\frac{\partial}{\partial X} + \frac{\partial Y}{\partial y}\frac{\partial}{\partial Y}, \tag{2.13}$$

$$\frac{\partial}{\partial \theta} = \frac{\partial X}{\partial \theta}\frac{\partial}{\partial X} + \frac{\partial Y}{\partial \theta}\frac{\partial}{\partial Y} + \frac{\partial}{\partial \Theta}. \tag{2.14}$$

The transformations (2.11)–(2.14) imply the total derivative operator (2.5) can be written

$$\frac{D}{Dt} = \frac{\partial}{\partial T} + u_g \frac{\partial}{\partial X} + v_g \frac{\partial}{\partial Y} + \dot{\theta}\frac{\partial}{\partial \Theta}. \tag{2.15}$$

Thus, (2.8) is still the fundamental predictive equation of the model but with the total derivative now given by (2.15). We can invert (2.12) and (2.13), which yields

$$\frac{\zeta}{f}\frac{\partial}{\partial X} = \frac{\partial Y}{\partial y}\frac{\partial}{\partial x} - \frac{\partial Y}{\partial x}\frac{\partial}{\partial y}, \tag{2.16}$$

and

$$\frac{\zeta}{f}\frac{\partial}{\partial Y} = -\frac{\partial X}{\partial y}\frac{\partial}{\partial x} + \frac{\partial X}{\partial x}\frac{\partial}{\partial y}. \tag{2.17}$$

We can use (2.16) and (2.17) in (2.14), along with the Jacobian relations (2.7), to obtain

$$\zeta\frac{\partial}{\partial \Theta} = \xi\frac{\partial}{\partial x} + \eta\frac{\partial}{\partial y} + \zeta\frac{\partial}{\partial \theta}. \tag{2.18}$$

We see from (2.18) that the term "vortex coordinates" can reasonably be applied to the geostrophic coordinates, since the partial theta-derivative in transformed space is along the three dimensional absolute vorticity vector in (x, y, θ) space.

An important aspect of the geostrophic momentum approximation is that the essential conservation relations of the primitive equations are maintained in their original form.

For example, conservation of potential temperature is formally identical to the primitive equation form, but with the total derivative given by (2.15); a similar statement holds for the energy equation as well.

It is easy to imagine from the form of the potential density equation that its inverse, the potential vorticity equation, will be formally identical to the primitive equation form of the potential vorticity equation. In fact, the potential vorticity equation is derived in the same manner as the potential density equation (2.8). Thus, combining (2.4) and (2.6) can also yield

$$\frac{Dq}{Dt} - \frac{1}{\sigma}\left(\xi\frac{\partial}{\partial x} + \eta\frac{\partial}{\partial y} + \zeta\frac{\partial}{\partial \theta}\right)\dot{\theta} = 0, \tag{2.19}$$

where $q = \zeta/\sigma$ is the Rossby-Ertel Potential Vorticity. Notice that in (x, y, θ), only the vertical component of vorticity contributes to the potential vorticity[1] equation or, in the case of (2.8), the potential density equation . The reason for this is related to the fact that (2.6) can be written in the form

$$\frac{\partial (\sigma q)}{\partial t} + \frac{\partial \left(u\sigma q - \dot{\theta}\xi\right)}{\partial x} + \frac{\partial \left(v\sigma q - \dot{\theta}\eta\right)}{\partial y} = 0,$$

so that intuitively we see that what Haynes and McIntyre (1987) proved for the isentropic form of the primitive equations holds as well when the geostrophic momentum approximation is made; namely, isentropes are semi-impermeable to potential vorticity (hence, to potential density also) in the sense that there can be no net transport of q across any isentrope. Applying (2.18) to (2.19) yields

$$\frac{Dq}{Dt} - \frac{\zeta}{q}\frac{\partial \dot{\theta}}{\partial \Theta} = 0, \tag{2.20}$$

which is again considerably simpler than its counterpart in (x, y, θ). Similarly, we can write (2.8) in the form

$$\frac{D\sigma^*}{Dt} + \sigma^*\frac{\partial \dot{\theta}}{\partial \Theta} = 0. \tag{2.21}$$

---

[1] This vorticity quantity is more properly referred to as the *isentropic* vorticity ζ_θ, to be distinguished from the vertical vorticity component in pressure or height coordinates. However, we will keep the convention of using the symbol ζ when referring to the vertical vorticity component in all systems.

Already, important features of geostrophic coordinates are apparent. In addition to the simplicity of, for example, (2.20), the Jacobian of the transformation from physical coordinates is simply the dimensionless vertical component of absolute vorticity ζ/f (compare (2.12) and (2.13) with (2.7)). Second, horizontal advecting velocities have become geostrophic, which eliminates the need to solve an additional equation to close the system in the adiabatic case, yet the governing equations implicity retain the ageostrophic advections. In our two-dimensional frontogenesis model, σ^* will be the predicted quantity.

2.2.2 Invertibility Principle

Because prediction of σ^* can now be performed in geostrophic coordinate space, in order to form a closed system we need to follow the procedure of Schubert *et al.* (1989) and formulate the invertibility relation alluded to above in transformed space also. It can be shown that the geostrophic and hydrostatic relations in (X, Y, Θ) take the form

$$(fv_g, -fu_g, \Pi) = \left(\frac{\partial M^*}{\partial X}, \frac{\partial M^*}{\partial Y}, \frac{\partial M^*}{\partial \Theta}\right),$$
(2.22)

which is identical to the form taken in (x, y, θ) space with M replaced by M^*, where

$$M^* = M + \tfrac{1}{2}\left(u_g^2 + v_g^2\right)$$
(2.23)

is the Bernoulli function. The potential density σ^* is a combination of the mass field σ and the wind field ζ. However, σ is related to Π, and using (2.7) ζ can be expressed in terms of u_g and v_g. By (2.22), then, the wind and mass fields can be obtained from σ^* if we can somehow invert it to obtain M^*. This second order partial differential equation, along with appropriate boundary conditions, is usually referred to as the invertibility principle. A relation between M^* and σ^* can be derived as follows. From the definition of σ^* we have

$$\frac{f}{\zeta}\frac{\partial \Pi}{\partial \theta} + \Gamma\sigma^* = 0,$$
(2.24)

where $\Gamma = d\Pi/dp = \kappa\Pi/p$. This last equation can be written

$$\frac{\partial(x, y, \Pi)}{\partial(X, Y, \Theta)} + \Gamma\sigma^* = 0.$$
(2.25)

Expressing x and y in terms of u_g and v_g by (2.10), and then using (2.22), we can write (2.25) as

$$\left(f^2 - \frac{\partial^2 M^*}{\partial X^2}\right)\left(\frac{\partial^2 M^*}{\partial Y \partial \Theta}\right)^2 + \left(f^2 - \frac{\partial^2 M^*}{\partial Y^2}\right)\left(\frac{\partial^2 M^*}{\partial X \partial \Theta}\right)^2 + 2\left(\frac{\partial^2 M^*}{\partial X \partial Y}\right)\left(\frac{\partial^2 M^*}{\partial Y \partial \Theta}\right)\left(\frac{\partial^2 M^*}{\partial \Theta \partial X}\right)$$

$$+ \left\{ f^2 \left(f^2 - \frac{\partial^2 M^*}{\partial X^2} - \frac{\partial^2 M^*}{\partial Y^2} \right) + \left(\frac{\partial^2 M^*}{\partial X^2}\right)\left(\frac{\partial^2 M^*}{\partial Y^2}\right) - \left(\frac{\partial^2 M^*}{\partial X \partial Y}\right)^2 \right\} \frac{\partial^2 M^*}{\partial \Theta^2}$$

$$+ f^4 \Gamma \sigma^* = 0. \tag{2.26a}$$

If the upper boundary is an isentropic and isobaric surface with potential temperature Θ_T and Exner function Π_T, the upper boundary condition for (2.26a) is simply

$$\frac{\partial M^*}{\partial \Theta} = \Pi_T \qquad \text{at} \qquad \Theta = \Theta_T. \tag{2.26b}$$

If we neglect the effects of topography and assume that the lower boundary is both the constant isobaric height surface $\phi = 0$ and the isentropic surface $\Theta = \Theta_B$, then $M = \Theta\Pi$ at $\Theta = \Theta_B$. Written in terms of M^*, this lower boundary condition becomes

$$\Theta\frac{\partial M^*}{\partial \Theta} - M^* + \frac{1}{2f^2}\left[\left(\frac{\partial M^*}{\partial X}\right)^2 + \left(\frac{\partial M^*}{\partial Y}\right)^2 \right] = 0 \qquad \text{at} \qquad \Theta = \Theta_B. \tag{2.26c}$$

The lateral boundary conditions depend on the particular application and will be discussed later in the context of the two dimensional model. It should be noted here that defining the lower boundary as both isobaric and isentropic does not necessarily exclude formation of a surface front; however, in Chapter 4 we prescribe these boundaries to be constant surfaces of potential density; in this case, as noted by Keyser *et al.* (1986), the possible coupling effects between surface and upper-level fronts (through vertical motions) are excluded.

Equations (2.8), (2.22) and (2.26) form a closed system. The computational scheme is as follows: knowing σ^*, solve (2.26) for M^*; use (2.22) to compute u_g and v_g; use these geostrophic winds in (2.8) to predict a new σ^*.

Chapter 3

FRONTOGENESIS BY HEIGHT DEPENDENT DEFORMATION

3.1 Two Dimensional Model

3.1.1 Theory

So far, using both the geostrophic momentum approximation and a useful coordinate transform, we have reviewed the necessary three dimensional theory to study a wide range of fluid phenomena which are too general to be studied with quasigeostrophic theory; however, we have at the same time retained its major benefits, such as the balance relationships in the resulting equations which are necessary to recover the fields of interest. We now apply a simplified version of this theory to study upper level (i.e. internal) frontogenesis. In particular, we assume the motions to be adiabatic, and we simplify to two dimensions both the potential density equation and the invertibility relation arrived at in Chapter 2 in order to study the frontogenesis process in the transverse (X,Θ) plane. The assumption that no variations in the fields of interest occur along the front follows a frequently held axiom that the relationship between such variations and the frontogenesis process itself is not clear, but that such an assumption is acceptable for along-front geostrophic flows (i.e. transverse geostrophy) where the front is assumed to be straight and variations of the along-front fields are small.

Let us now generalize the two-dimensional frontogenesis problem of Hoskins (1971, 1972) and Hoskins and Bretherton (1972). In this case, fronts oriented in the y-direction are assumed to be forced by a pure, height *dependent* deformation field so that

$$u_g(x,\theta) \;=\; -\alpha(\theta)\,x, \tag{3.1}$$

$$v_g(x,y,\theta,t) \;=\; \alpha(\theta)\,y + v'_g(x,\theta,t), \tag{3.2}$$

where $\alpha = \alpha(\theta)$ is the vertically varying deformation rate, the first terms on the right hand side represent the fixed (or "slowly" varying) deformation field, and the v_g' term represents the rotational flow generated during frontogenesis so that $v_g'(x,\theta,0) = 0$.

Since we assume that motions along the front are geostrophic, the entire secondary circulation is in the transverse plane and is given by u_a. We can easily recover this circulation; from the definition $u = Dx/Dt$, equations (2.10), the geostrophic relation (2.22), the assumption (3.1), and the fact that $u_a = u - u_g$, we have

$$u_a = \frac{1}{f^2}\left[\frac{\partial}{\partial T}\frac{\partial M^*}{\partial X} - \alpha X\frac{\partial^2 M^*}{\partial X^2}\right]. \tag{3.3}$$

3.1.2 Governing Equations

Now we formulate the two dimensional invertibility principle in a manner consistent with the requirements of the numerical solver which is discussed later. First, however, we reduce our fundamental predictive equation (2.8) to two dimensions in geostrophic and isentropic space. Setting

$$\frac{\partial}{\partial y} = \frac{\partial X}{\partial y}\frac{\partial}{\partial X} + \frac{\partial Y}{\partial y}\frac{\partial}{\partial Y} = 0$$

with respect to the field variables, using the definitions (2.10) and the assumptions (3.1) and (3.2), we obtain

$$\frac{\partial}{\partial Y} = -\frac{\alpha}{f}\frac{\partial}{\partial X}. \tag{3.4}$$

Using the adiabatic assumption $\dot\theta = 0$ and substituting (3.4) into (2.15) transforms our total derivative operator into

$$\frac{D}{Dt} = \frac{\partial}{\partial T} - \alpha X\frac{\partial}{\partial X}, \tag{3.5}$$

so that equation (2.8) becomes

$$\frac{\partial \sigma^*}{\partial T} - \alpha X\frac{\partial \sigma^*}{\partial X} = 0, \tag{3.6}$$

which has as its solution

$$\sigma^*(X,\Theta,T) = \sigma_I^*\left(Xe^{\alpha T},\Theta\right). \tag{3.7}$$

Substituting (3.4) into (2.26a), we obtain the corresponding two-dimensional invertibility relation

$$\left(1 + \frac{\alpha^2}{f^2}\right) \left[\left(\frac{\partial^2 M^*}{\partial \Theta \partial X}\right)^2 - \frac{\partial^2 M^*}{\partial X^2}\frac{\partial^2 M^*}{\partial \Theta^2}\right] + f^2\left(\frac{\partial^2 M^*}{\partial \Theta^2} + \Gamma\sigma^*\right) = 0.$$

Since α is coupled to T in the prediction of σ^*, only the product of these quantities is important; in particular, we can make α as small as is convenient for our purposes. If we choose α so that $\alpha^2/f^2 \ll 1$, then we can approximate the above as

$$\frac{\partial^2 M^*}{\partial \Theta^2}\left(f^2 - \frac{\partial^2 M^*}{\partial X^2}\right) + \left(\frac{\partial^2 M^*}{\partial \Theta \partial X}\right)^2 + f^2\Gamma\sigma^* = 0, \qquad (3.8a)$$

which, interestingly, is identical to the form obtained for both the specific case where α is considered constant, and for the case study of the atmospheric response to a moving squall line (Schubert et $al.$ 1989) where both the zonal geostrophic and meridional ageostrophic components of the wind are assumed to be zero. The upper boundary condition is unchanged:

$$\frac{\partial M^*}{\partial \Theta} = \Pi_T \qquad \text{at} \qquad \Theta = \Theta_T, \qquad (3.8b)$$

and from (2.26c) and (3.4) the lower boundary condition becomes

$$\Theta\frac{\partial M^*}{\partial \Theta} - M^* + \frac{1}{2f^2}\left(\frac{\partial M^*}{\partial X}\right)^2 = 0 \qquad \text{at} \qquad \Theta = \Theta_B, \qquad (3.8c)$$

where we again use the constraint $\alpha^2/f^2 \ll 1$. For the lateral boundary condition we make use of the fact that the geostrophic deformation field (3.1) and (3.2) implies $v_g \rightarrow 0$ as $X \rightarrow \pm\infty$. In the model, this last expression will be approximated by

$$M^*(\Theta, T) = M^*(\Theta, 0) \qquad \text{at} \qquad X = -X_L, 3X_L, \qquad (3.8d)$$

where we use the definition (2.22) and define X_L as a (variable) scale width of the domain of interest (see the numerical procedures section).

From a practical standpoint, we can see that already our two dimensional model is much simpler to solve and requires less computer time due to the analytic form of the solution (3.7). The advecting velocity in (3.6) is simply the product of the independent variable X and the deformation rate α, which is prescribed as varying only in the vertical;

therefore, we need not diagnose M* in order to determine this advection quantity as we did for the three dimensional case. Thus, in two dimensional (X, Θ) space our computational scheme is as follows: knowing σ^*, use (3.8) to diagnose M* only for those time steps for which we wish to determine the wind and mass fields. To recover the transverse ageostrophic circulation requires diagnosing M* for three successive time steps in order to make use of a discretized version of (3.3).

We should point out that an important limitation of our two-dimensional model results by neglecting along-front temperature gradients. Keyser and Pecnick (1985) have shown these gradients to be significant in the formation of some upper fronts. From this point of view, then, our results should be taken within the constraints of the assumptions made when formulating the simplified model presented here.

3.2   Procedure for the Invertibility Solver

Our two dimensional model has been reduced to (3.6) and (3.8), the former having an analytical solution given by (3.7). The numerical solution to the nondimensional form of (3.8) developed below will be given by the Full Multigrid (FMG) solver of Fulton (1989), an efficient program utilizing nonlinear Gauss-Seidel relaxation for smoothing. The FMG program requires that $\mathcal{M}(X, \Theta) = M^*(X, \Theta) - \overline{M}^*(\Theta)$ be a specified value on each lateral boundary; that is, the model requires Dirichlet lateral boundary conditions[1]. For a more in-depth discussion of the invertibility solver the reader is referred to Fulton (1989).

To rewrite our diagnostic equation (3.8) in the nondimensional form needed, we introduce the nondimensional coordinates (it should be noted that these are quite different from the physical coordinates x and z)

$$x = \frac{f}{c}X, \qquad z = \frac{\Theta - \Theta_B}{\Theta_T - \Theta_B}, \tag{3.9}$$

---

[1] Here, $\overline{M}^*$ is a horizontally averaged value of M* and $\mathcal{M}$ is a deviation value. To determine an appropriate value for $\overline{M}^*$, note that by integrating (3.13) we can write a basic state form of the initial pressure field. Integration of the hydrostatic relation (2.22) and the definition of Π, then, will define a value of $\overline{M}^*$ for any point.

with $c = [aR(\Theta_T - \Theta_B)]^{1/2}$, $a = (p_B - p_T)/p_B$, and R the gas constant for dry air. Derivatives between these nondimensional quantities and those in geostrophic space are then related by

$$\frac{\partial}{\partial X} = \frac{f}{c}\frac{\partial}{\partial x}, \qquad \frac{\partial}{\partial \Theta} = \frac{1}{(\Theta_T - \Theta_B)}\frac{\partial}{\partial z} . \qquad (3.10)$$

Now we write (3.8) in its nondimensional form: nondimensionalizing $\mathcal{M}$ by c^2, σ^* by σ_0 (defined in the next section), Γ by $\Gamma_0 = R/p_B$, Π by c_p, and p by p_B, and retaining the original notation for these quantities yields

$$\left(1 - \frac{\partial^2\mathcal{M}}{\partial x^2}\right)\left(\overline{\Gamma\sigma} - \frac{\partial^2\mathcal{M}}{\partial z^2}\right) - \left(\frac{\partial^2\mathcal{M}}{\partial z\partial x}\right)^2 = \Gamma\sigma^* , \qquad (3.11a)$$

$$\frac{\partial\mathcal{M}}{\partial z} = 0 \quad \text{at} \quad z = 1 , \qquad (3.11b)$$

$$\mathcal{M} - b\frac{\partial\mathcal{M}}{\partial z} - \frac{1}{2}\left(\frac{\partial\mathcal{M}}{\partial x}\right)^2 = 0 \quad \text{at} \quad z = 0 , \qquad (3.11c)$$

$$\mathcal{M} = 0 \quad \text{at} \quad X = -X_L , 3X_L , \qquad (3.11d)$$

where $b = \Theta_B/(\Theta_T - \Theta_B)$. Second-order centered finite differencing is used for both (3.11a) (the domain interior), and for (3.11b) and (3.11c) (the upper and lower boundary conditions) where ghost points satisfy the requirements of the finite difference scheme. Applying the homogeneous characteristics of the atmosphere outside the domain allows use of Dirichlet lateral conditions (discussed below) for the four ghost points on those boundaries. Once the $\mathcal{M}$-field has been diagnosed, M* may be easily found and, using (2.22), the wind and pressure fields calculated. Representation of the fields of interest in physical space can be made by using (2.10) once the geostrophic wind field has been calculated.

If there are nz vertical grid intervals, the vertical resolution is $\Delta\Theta = (\Theta_T - \Theta_B)/nz$ K. To determine the horizontal grid spacing, we first must examine the horizontal extent necessary to avoid contamination of the results by the lateral boundary conditions, defined as one Rossby length λ, where

$$\lambda = \frac{\Theta_T - \Theta_B}{f}\left[\frac{(R/p_B)(p_B - p_T)}{\Theta_T - \Theta_B}\right]^{\frac{1}{2}} . \qquad (3.12)$$

From this information we define $X_L = 2\lambda$, so that the domain is eight Rossby lengths wide. Although this domain size is somewhat cumbersome from a numerical standpoint, the realism of our results here demand that warm air border the cold trough on both sides. The asymmetry of the domain definition allows for a shifted deformation axis as described below. With our values for pressure and potential temperature given in the next section and f taken as 10^{-4} s^{-1}, $\lambda \doteq 1595$ km; the relatively large value for λ is a result of the depth of the domain. The horizontal resolution is given by $\Delta X = \lambda[\Delta\Theta/(\Theta_T - \Theta_B)]$. A typical value for nz is 64, which corresponds to $\Delta\Theta \doteq 1.56$ K and $\Delta X \doteq 25$ km.

3.3 Description of the Initial Domain

Equations (3.6) and (3.8) together with the geostrophic/hydrostatic relations (2.22) form a closed system; However, diagnosis of the wind and mass fields by (3.8) requires that the initial potential density field be prescribed in (X, Θ) space. To gain some insight as to the observed vertical variation of potential density, we derived the σ^* field using data from the U.S. Standard Atmosphere tables (1966) for the months of January and July. Based on this data, we define the initial pressure field as

$$
\text{P}_\text{I}(X, \Theta) = \text{P}_\text{T} + \left\{ \frac{\left(\frac{\Theta_T - \Theta}{\Theta_T - \Theta_B}\right)(\text{P}_\text{B} - \text{P}_\text{T}) + (\delta\Theta\delta\sigma)\ln A}{\text{P}_\text{B} - \text{P}_\text{T} + (\delta\Theta\delta\sigma)\ln B} \right\} (\text{P}_\text{B} - \text{P}_\text{T}) \ , \qquad (3.13)
$$

for which the initial potential density field [2] is

$$
\sigma_\text{I}(X, \Theta) = \frac{\sigma_0 - (\delta\sigma)\tanh\left(\frac{\Theta - \hat{\Theta}_\text{I}}{\delta\Theta}\right)}{1 + \left(\frac{\delta\Theta\delta\sigma}{\text{P}_\text{B} - \text{P}_\text{T}}\right)\ln B} \ , \qquad (3.14)
$$

---

[2] The relationship between the initial fields of pseudo-density and potential pseudo-density is found as follows: with the geostrophic components as defined above in (3.1) and (3.2), we know initially that

$$
\frac{\partial u_g}{\partial x} = -\alpha, \qquad \frac{\partial u_g}{\partial y} = 0, \qquad \frac{\partial v_g}{\partial x} = \frac{\partial v_g'}{\partial x} = 0, \qquad \text{and} \qquad \frac{\partial v_g}{\partial y} = \alpha,
$$

so that using (2.7) we can write $\zeta_\text{I} = f - \alpha^2/f \doteq f$. Thus, from the definition $\sigma^* = (f/\zeta)\sigma$ we can say with a high degree of accuracy that *initially* the potential density field and the density field are equivalent in the domain, and the two quantities are essentially interchangeable. In addition, the condition (3.8d) implies that in the far field and for all time $M^* \neq F(X)$, so we have exactly $\zeta = f$ and $\sigma^* = \sigma$ outside the domain.

where

$$A = \left[\frac{\cosh\left(\frac{\Theta - \hat{\Theta}_I}{\delta\Theta}\right)}{\cosh\left(\frac{\Theta_T - \hat{\Theta}_I}{\delta\Theta}\right)}\right], \qquad\qquad B = \left[\frac{\cosh\left(\frac{\Theta_B - \hat{\Theta}_I}{\delta\Theta}\right)}{\cosh\left(\frac{\Theta_T - \hat{\Theta}_I}{\delta\Theta}\right)}\right],$$

$\Theta_B = 280$ K, $\Theta_T = 380$ K, $p_B = 101575$ Pa, $p_T = 11575$ Pa, $\sigma_0 = (p_B - p_T)/(\Theta_T - \Theta_B) = 900$ Pa/K, $\delta\sigma = 800$ Pa/K, and

$$\hat{\Theta}_I = \begin{cases} \overline{\Theta} - (\Delta\Theta)\left[1 - \cos\left(\frac{\pi(X+X_L)}{2X_L}\right)\right] & -X_L \leq X \leq 3X_L, \\ \overline{\Theta} & X < -X_L \quad \text{or} \quad X > 3X_L, \end{cases} \qquad (3.15)$$

is the variation of potential temperature along the tropopause in the (X, Θ) plane. The quantity $\overline{\Theta} = 340$ K is a global average value of the tropopause potential temperature[3]. As can be seen in figures 3.1 and 3.2, with the above definitions the initial potential density field σ_I closely follows the observed annual average (an average of the January and July values) of σ. Although a more exact fitting to observations can be obtained, the values chosen here display the characteristic sharp decline of σ observed in regions favorable for frontogenesis—features which are smoothed out in the climatological averages depicted by the observations.

Thus, unlike the two layer model of Hoskins (1971), we prescribe a continuous potential vorticity (PV) field with a sharp vertical gradient in the vicinity of the tropopause. Notice that at the upper and lower boundaries (Θ_T and Θ_B), equation (3.13) reduces to the constant pressure surfaces p_T and p_B which satisfy our original boundary assumptions in equations (2.26b) and (2.26c). These lower boundary values were chosen as an annual average from the climatological data, and upper boundary values were chosen in such a way as to satisfy our desired value of σ_0. The parameter $\Delta\Theta$ in equation (3.15) controls the initial horizontal temperature gradient in the vicinity of the tropopause. In general terms, its numerical value is small in keeping with the approach of Hoskins that the assumed geostrophic deformation field is acting on a thermal gradient which is initially weak.

---

[3] Referring to figures 3.1 and 3.2, our assumed value compares acceptably well with observed tropopause temperatures. Thus, for the purposes of our model we consider the tropopause to have a globally averaged value equivalent to $\overline{\Theta}$, and within the domain of interest the tropopause lowers in conjunction with the initial horizontal thermal gradient in the interior.
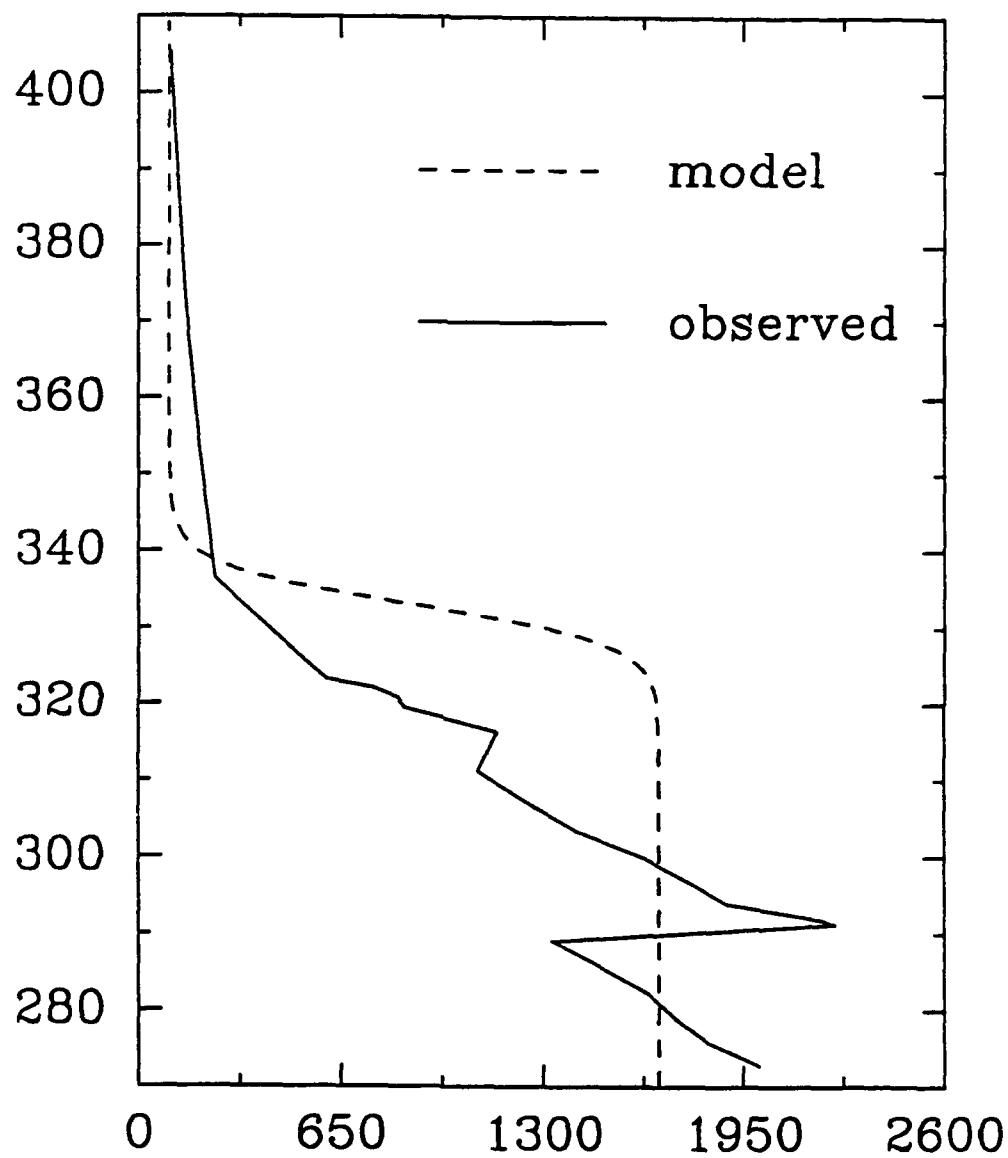
Figure 3.1: Potential density vs. potential temperature. Observed values are for the month of January as derived from the U.S. Standard Atmosphere tables. The dashed curve is the representation of equation (3.14) for a typical tropopause temperature. Un.'s on the horizontal axis are Pa/K.
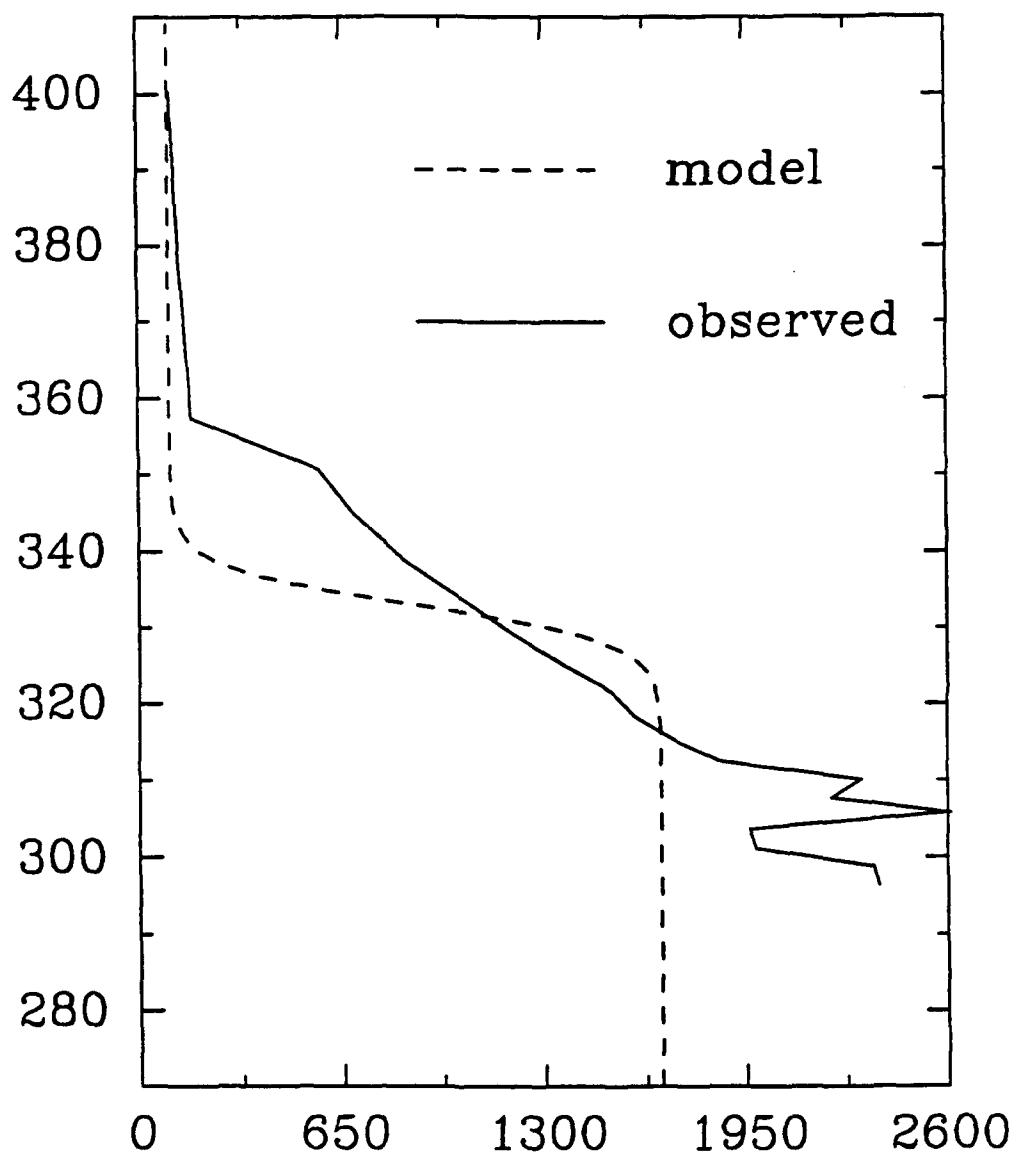
Figure 3.2: Same as figure 3.1, except for the month of July.

Thus, the tropopause has a trough representing colder air in the center of the domain in a manner similar to that of Hoskins *et al.* (1985).

Figures 3.3–3.6 show the initial state of the entire domain. In figure 3.3 the σ^* field is greatest at the surface and in the center of the domain below the upper trough. The associated potential vorticity field q is depicted in figure 3.4. From the definitions in Chapter 2, we have the relationship $q = f/\sigma^*$; since these two quantities are inversely proportional within the constant f, emphasis will be placed on the more familiar q-field.

Figure 3.5 confirms our earlier result with regard to the initial vorticity field; the initial meridional geostrophic wind field displayed in the figure indicates a very weak horizontal gradient so that, as stated earlier, the earth's vorticity is nearly equal to the absolute vorticity. Finally, figure 3.6 gives the temperature profile.

3.4 Results of the Model

3.4.1 Initial Results

Preliminary experiments conducted using a deformation rate which linearly decreased with height were unsuccessful at producing upper fronts. Desired major characteristics, most importantly a folding event, were not reproduced. Also, neither a linear nor Gaussian definition of α were successful when the zero zonal wind line (center of the deformation field) was placed in the center of the trough. As noted below, however, there was a marked improvement when the zero line was moved off to either the left or right midway between the cold and warm air. Observed features of baroclinic waves are consistent with this shift and serve as sufficient motivation; the existence of confluence in the entrance region of jet streaks is well documented both upstream and downstream of the associated upper trough, corresponding to a model shift left and right, respectively. It is in such regions that the bulk of observational data has been taken verifying upper frontogenesis and associated folding events.

3.4.2 Gaussian Deformation

Here the deformation field is shifted off the center of the domain to a point halfway between the coldest and warmest air. There are two such points: one corresponds to
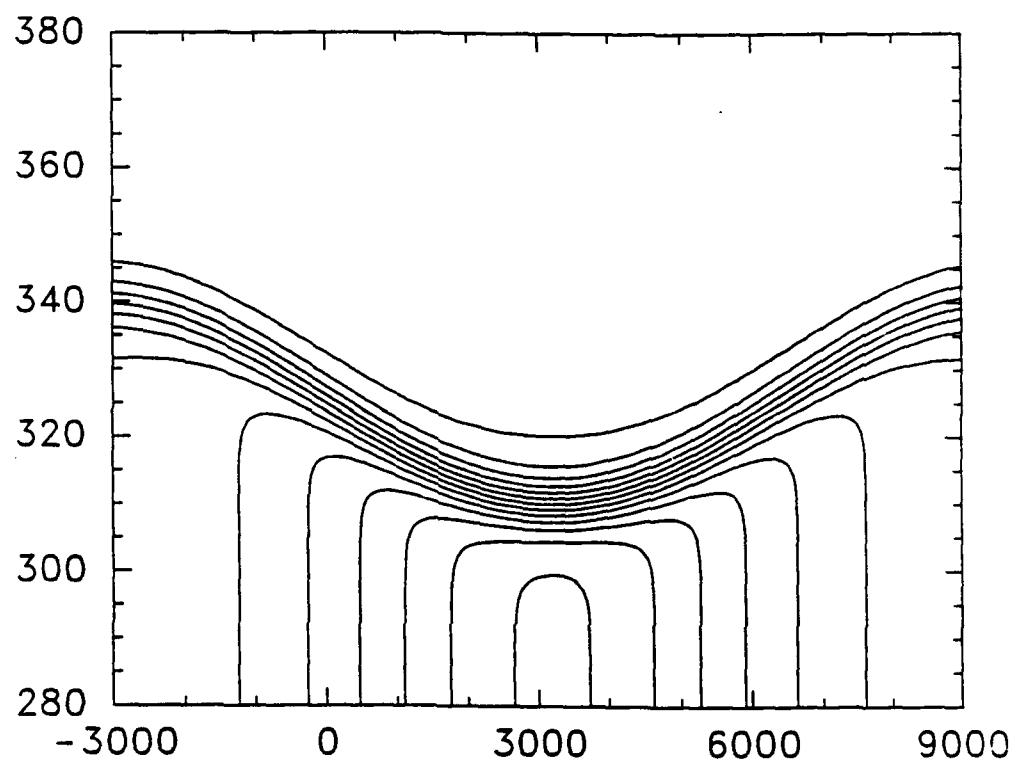
Figure 3.3: Initial potential density field in (X, Θ) space as derived from the FMG solver at $t = 0$. Isolines are every 200 Pa/K, with the top contour (smallest value) 200 and the bottom (largest) 2600. Distance is given in km on the horizontal axis.
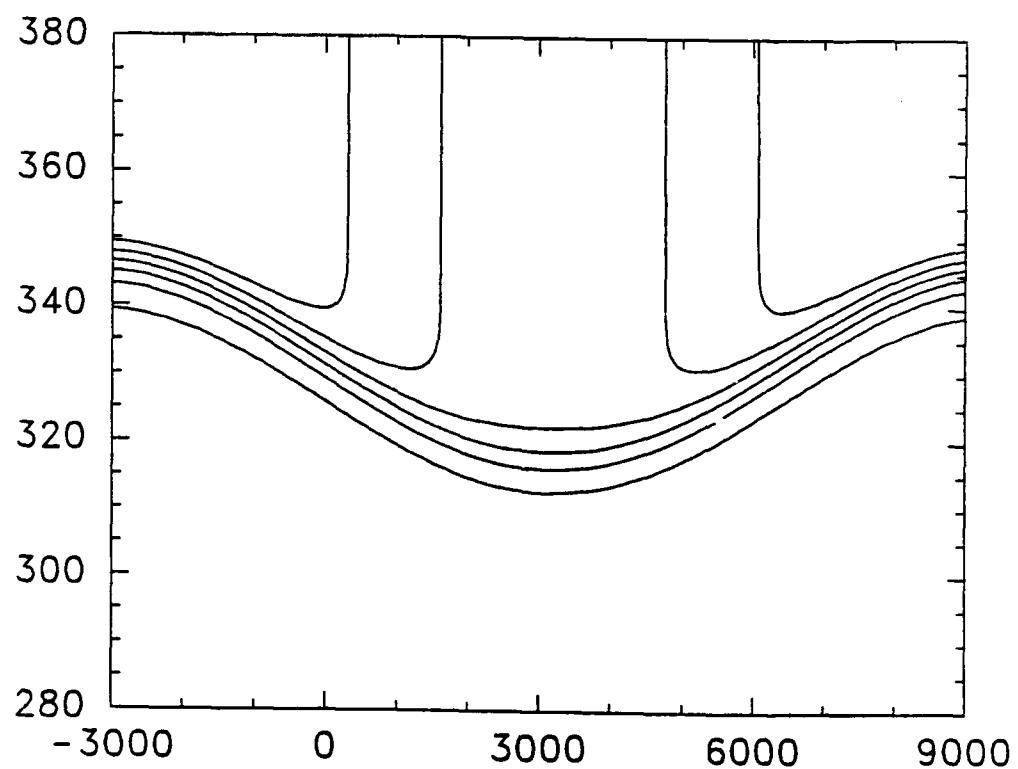
Figure 3.4: Initial potential vorticity field associated with figure 3.3. Units are 10^{-8} K/(Pa·s) with isolines every $15 \cdot 10^{-8}$ and bottom contour (smallest value) of $12 \cdot 10^{-8}$. Distance is given in km on the horizontal axis.
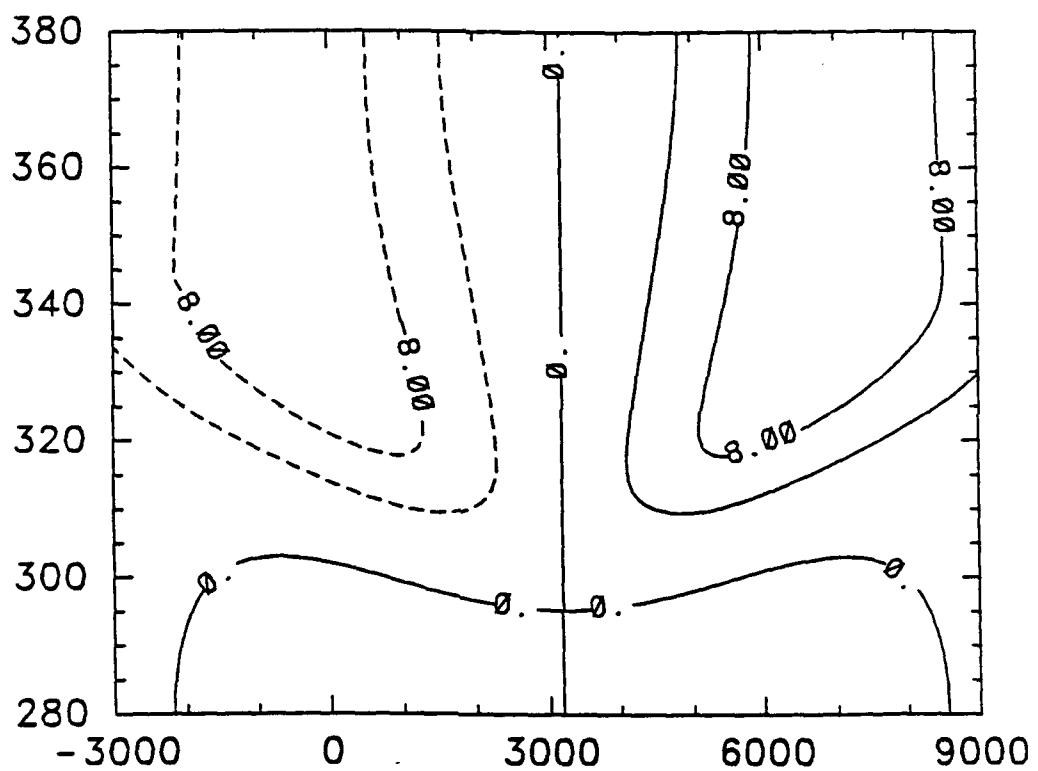
Figure 3.5: Initial meridional geostrophic wind field in (X, Θ) space as derived from the FMG solver. Dashed lines indicate winds from the north, solid lines from the south (m/s). Distance is given in km on the horizontal axis.
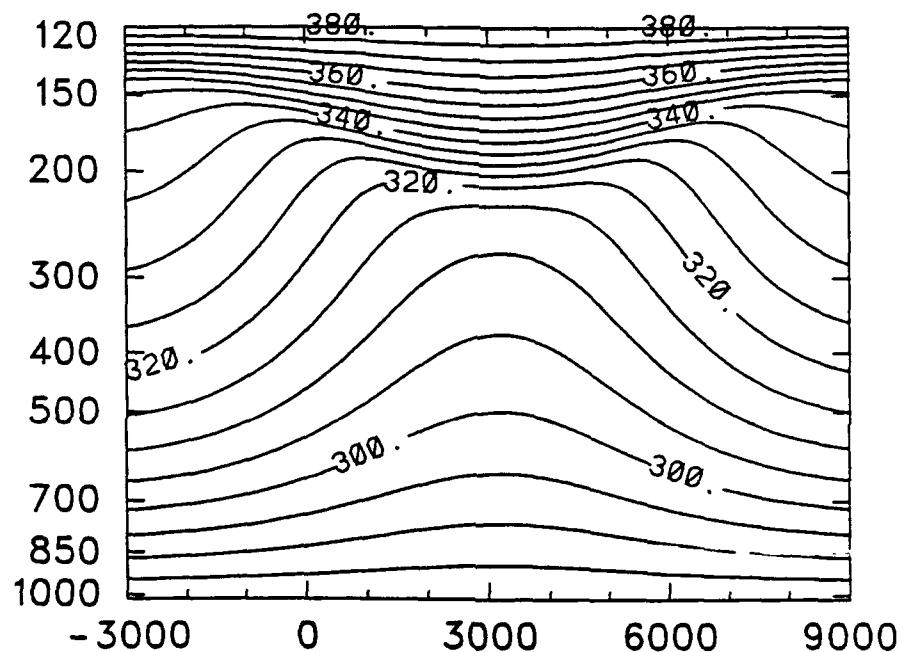
Figure 3.6: Initial potential temperature field in (x, p) space. Isentropes are every 5 K, ranging from the lower boundary value of 280 K to 380 K on the upper boundary. Distance is given in km on the horizontal axis.

X = 0, and the other to $X = 2X_L$. The shift provided by far the most realistic results of a folded dynamic tropopause.

In this experiment we set $\alpha = 10^{-5}\exp\{-(1/2)[(\Theta - \overline{\Theta})/\delta\Theta]^2\}$, where $\overline{\Theta}$ is the level of maximum deformation and $\delta\Theta$ is the e-folding half-depth of the α field. Typical values for these quantities were 330 K and 20 K, respectively. The coefficient 10^{-5} was chosen so that our assumption $(\alpha/f)^2 \ll 1$, which was used to arrive at the two-dimensional diagnostic equation, would be satisfied. The only consequence of such a procedure is more time must elapse to achieve the same results than would have been the case for a larger value of α. Although references to time can therefore only be made in a relative sense, we nevertheless prefer it to references to the product αT, which is somewhat more ambiguous since α varies with height.

Figure 3.7 shows that the folding process has already begun in the PV field at the 24 hour point. A jet along the front has rapidly developed, as shown in fig. 3.8 with maximum winds of about 44 m/s in the core near the tropopause. At the 36 hour point the folding process has intensified with a deeper region of anomalously high PV values contained in the developing upper front. The associated jet streak has increased slightly in magnitude (figs. 3.9, 3.10). After 48 hours a well developed folding of the PV field has occurred; figs. 3.11 and 3.12 show the PV field in geostrophic and physical space, respectively, at this time. There are several noteworthy features in comparing the two figures. First, the region above the fold and in the vicinity of the tropopause is shown to have a tighter gradient in physical space, which more closely matches observations of a near discontinuity of the PV field near the tropopause. Below, the fold itself displays the same characterisitic, and is also more narrow. In addition, the shift back to physical space has increased the horizontal extent of the fold by moving points near the jet farther west than corresponding points lower in the troposphere. All of these features are a result of the horizontal and vertical wind shear which, of course, is greatest near the jet. Figs. 3.13 and 3.14 show the wind field at 48 hours, also in geostrophic and physical space. A more realistic (stronger) wind shear pattern results from the shift. In general, the entire region of frontogenesis has been tightened due to its cyclonic nature. The characteristic of
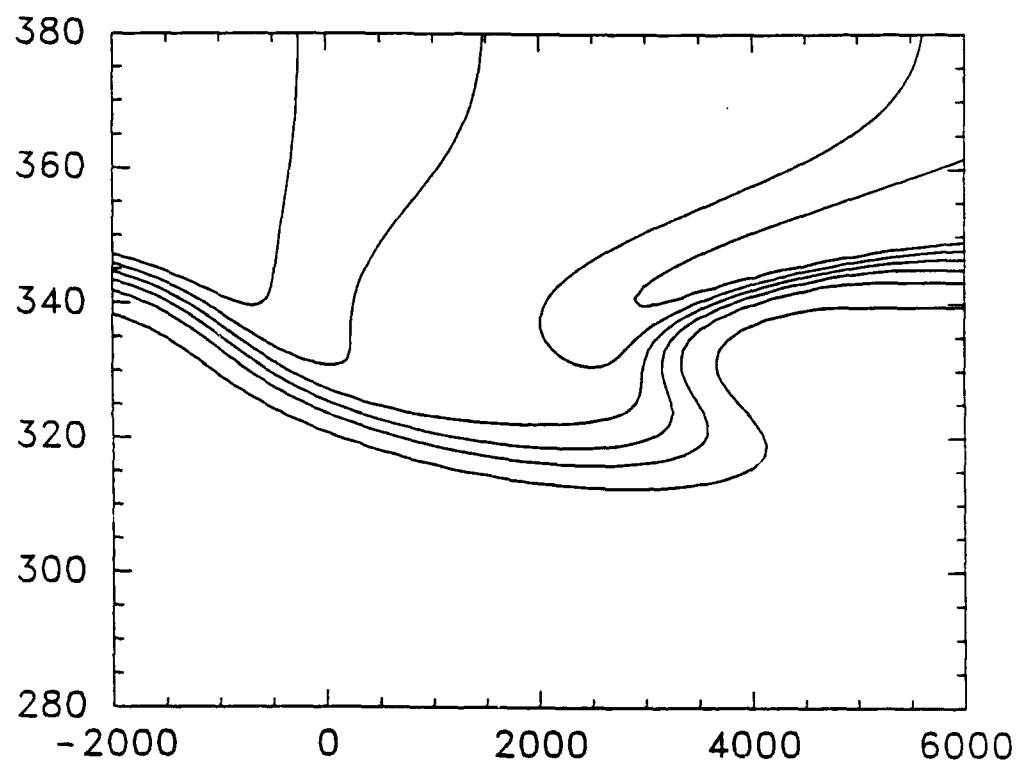
Figure 3.7: Potential vorticity field (10^{-8} K/(Pa·s)) at 24 hours in (X, Θ) space with isolines every $15 \cdot 10^{-8}$ and bottom (smallest) value of $12 \cdot 10^{-8}$. Distance on the horizontal axis is in km.
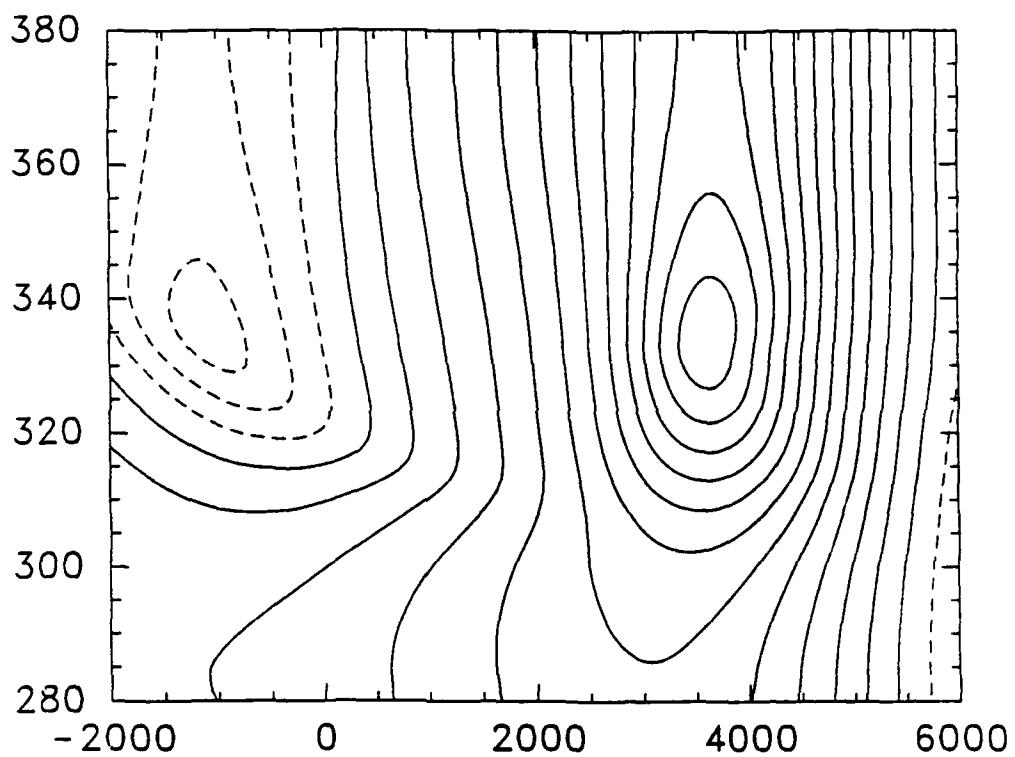
Figure 3.8: Meridional geostrophic wind field at 24 hours in (X, Θ) space. Strongest northerly winds are 12 m/s, with a southerly jet core of 44 m/s (isotachs every 4 m/s). Distance on the horizontal axis is in km.
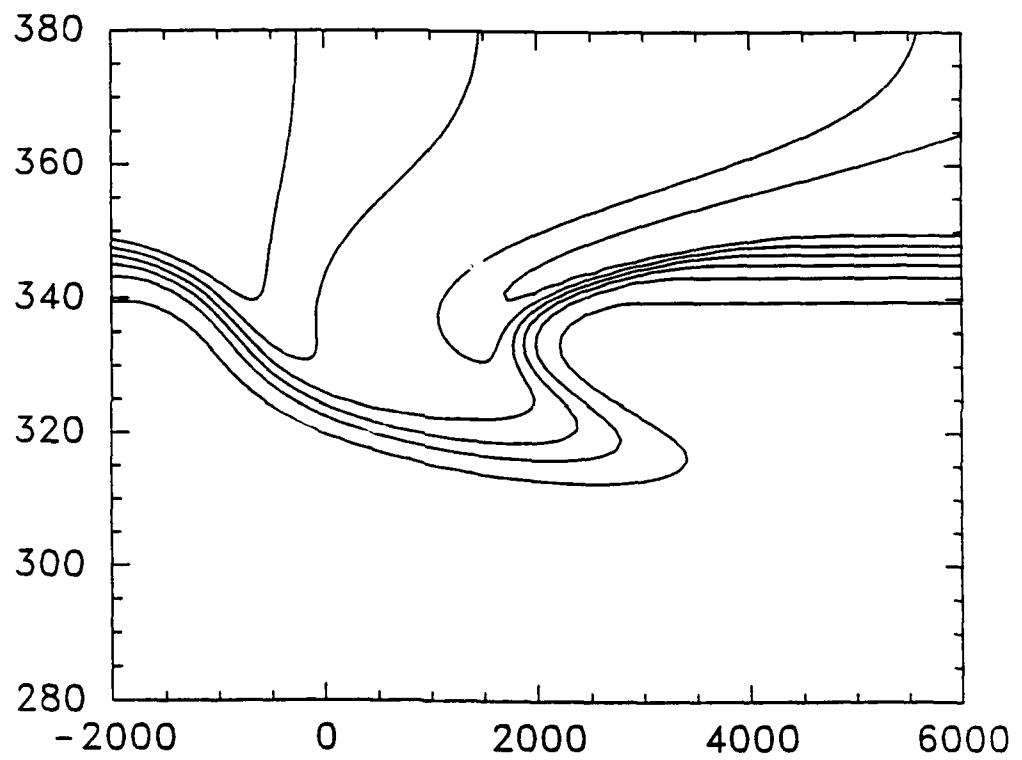
Figure 3.9: Potential vorticity field (10^{-8} K/(Pa·s)) at 36 hours in (X, Θ) space with isolines as in fig. 3.7. Distance is in km on the horizontal axis.
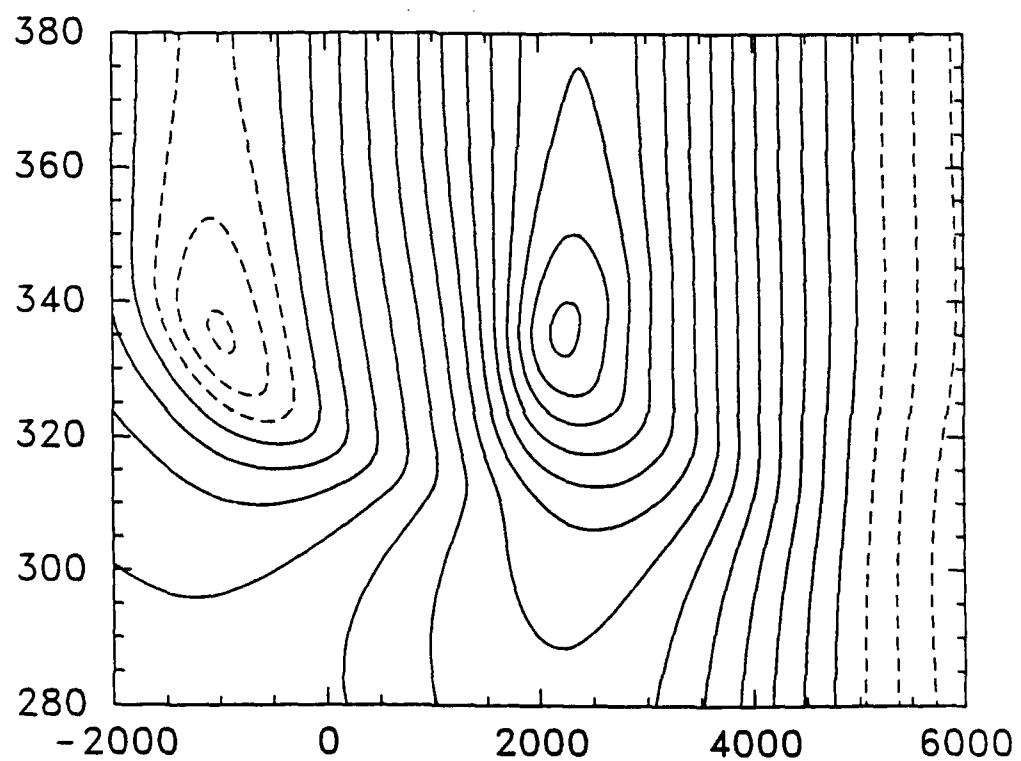
Figure 3.10: Meridional geostrophic wind field at 36 hours in (X, Θ) space. Isotachs are every 4 m/s. Strongest northerly winds (dashed) are 12 m/s, with a southerly jet core of 48 m/s. Distance is in km on the horizontal axis.
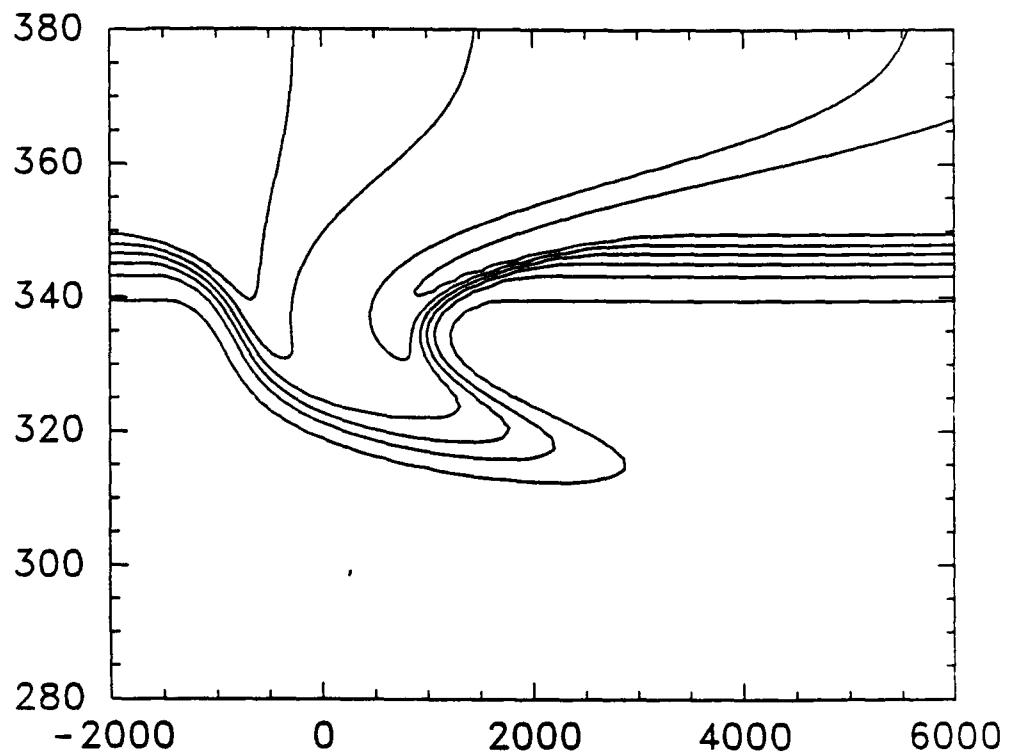
Figure 3.11: Potential vorticity field (10^{-8} K/(Pa·s)) at 48 hours in geostrophic space. Distance is in km on the horizontal axis, and isolines are as in figure 3.7.
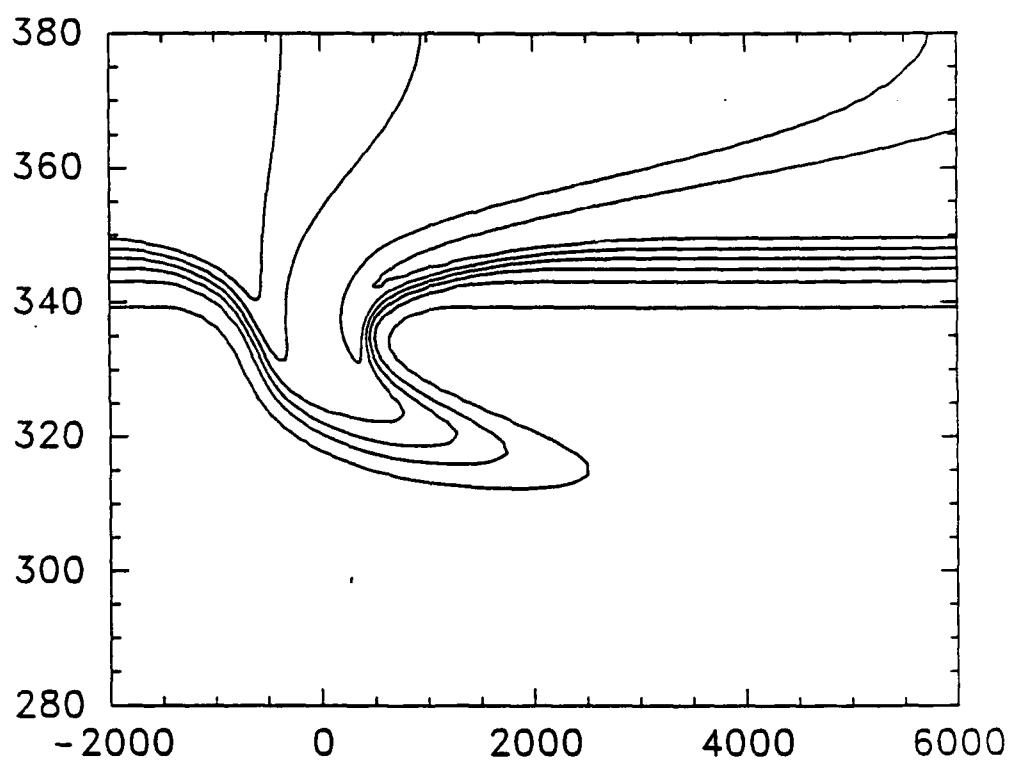
Figure 3.12: Potential vorticity field (10^{-8} K/(Pa·s)) at 48 hours in physical space. Distance is in km on the horizontal axis, and isolines are as in figure 3.7.

shrinking low pressure regions and broadening high pressure (anticyclonic) regions has, as stated previously, been well documented by numerous authors of semigeostrophic theory.

Figs. 3.15–3.17 and 3.18–3.20 are time sequences of the folding event; the first sequence shows the relationship between the tropopause fold and thermal field, and the second the relationship between the fold and associated jet. Perhaps the most important feature of these time series is their general agreement with the growing base of observational data (e.g. Shapiro, 1987). In these diagrams we see clearly the evolution from the initial trough of cold air shown in figs. 3.3–3.6, to a lowering of the tropopause, and finally to a narrow, deepening front with a statically stable layer, significant vertical motion along isentropic surfaces through the fold, and wind shearing in the vicinity of the front and jet streak. At the 48 hour point especially there is a characteristically thin layer of stratospheric air within the fold bounded both above and below by tropospheric air.

Our reproduction of upper frontogenesis processes in the absence of an initial surface temperature gradient confirms previous results of, for example, Buzzi et al. (1981). Fig. 3.21 shows perhaps more clearly than previous diagrams the extent of upper frontogenesis obtainable when the deformation field varies vertically. Among the most notable features of the model is the folded tropopause associated with the internal front. The realism of the folding process, as well as the horizontal wind shears developed near the jet core, are enhanced by the use of the geostrophic horizontal coordinate. Such increased resolution of field parameters has been documented before by Hoskins and West (1979), for example, but not as applied in the current results. Other recurrent features include the adiabatic exchange between troposphere and stratosphere through the fold, and a realistic jet stream in terms of both proximity to the front and intensity. These features taken together are remarkably similar to observations of, for example, Shapirc (1985), where an upper front containing primarily stratospheric air is bounded both above and below by tropospheric air. The fact that nearly adiabatic motion occurs through the model-produced fold reinforces the notion that anomalous lamina of ozone can be injected to the troposphere through such a tropopause folding event (Danielsen, 1980).
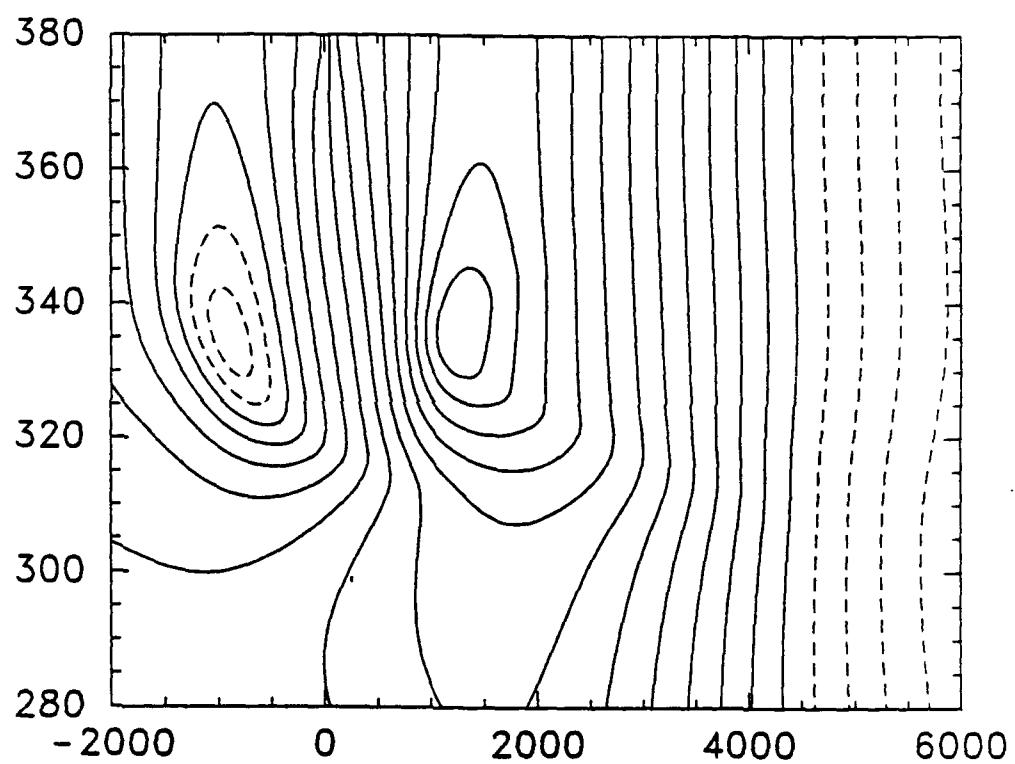
Figure 3.13: Meridional geostrophic wind field at 48 hours in geostrophic space. Strongest winds are 8 m/s from the north (dashed) and 44 m/s from the south, with isotachs every 4 m/s. Distance is in km on the horizontal axis.
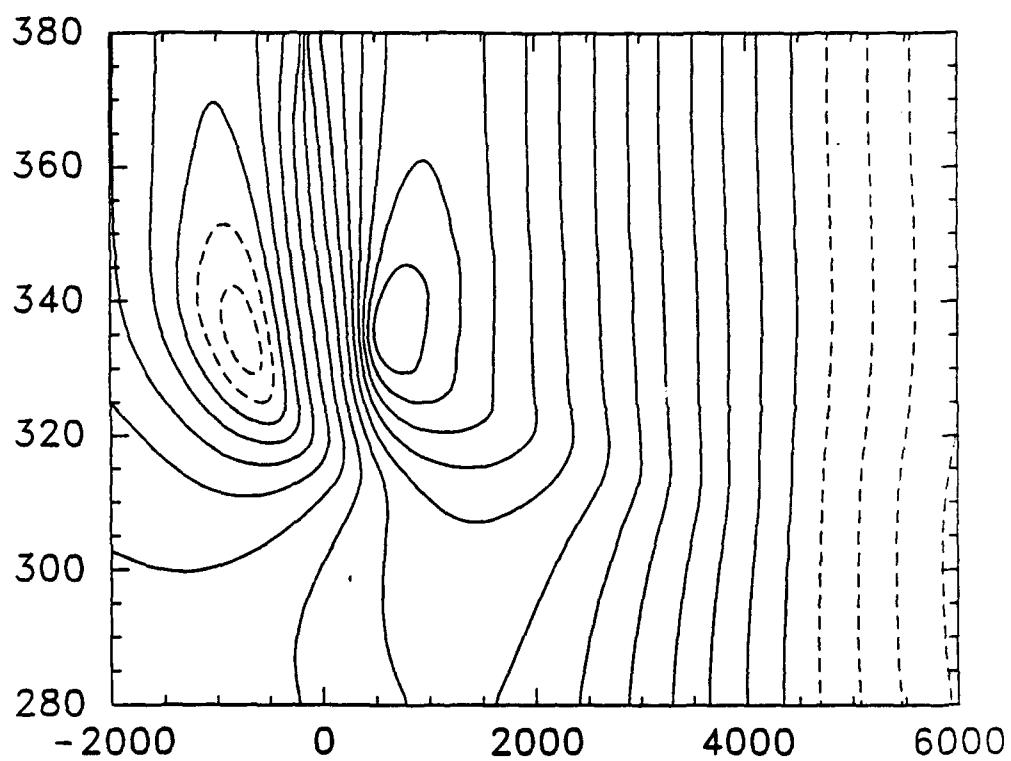
Figure 3.14: Meridional geostrophic wind field at 48 hours in physical space. Strongest winds are 8 m/s from the north (dashed) and 44 m/s from the south, with isotachs every 4 m/s. Distance is in km on the horizontal axis.
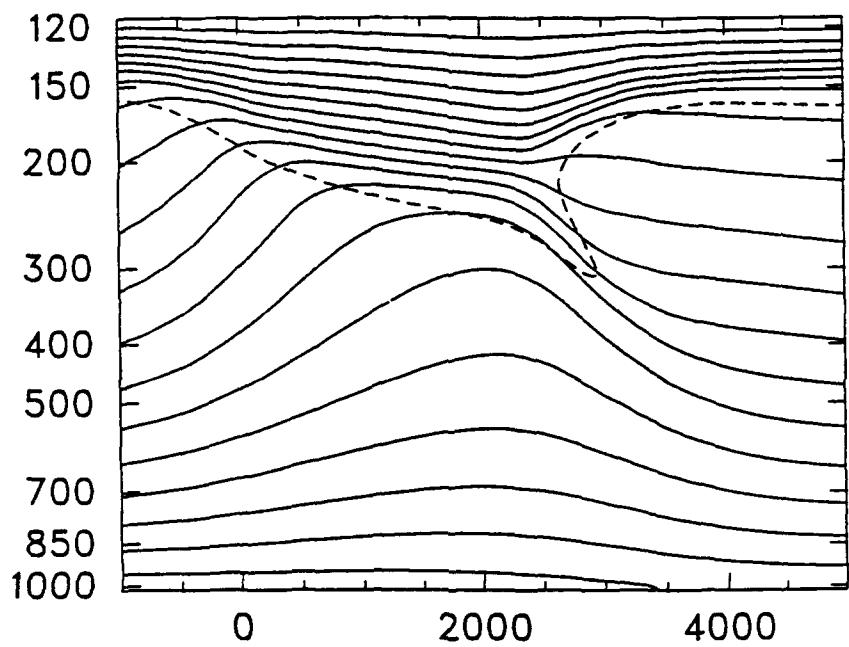
Figure 3.15: Thermal field at 24 hours in physical space with pressure (mb) as the vertical coordinate. The lowest isotherm is 285 K with increments of 5 K. Dashed line is the constant PV line $2 \cdot 10^{-7}$ K/(Pa·s), representing the dynamic tropopause. Distance is in km on the horizontal axis.
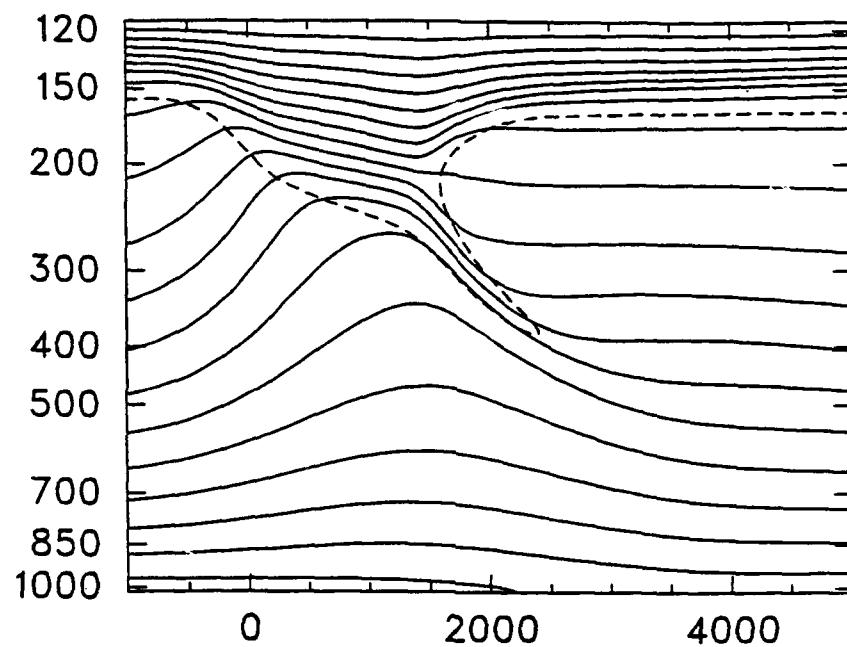
Figure 3.16: Same as fig. 3.15, except for 36 hours.
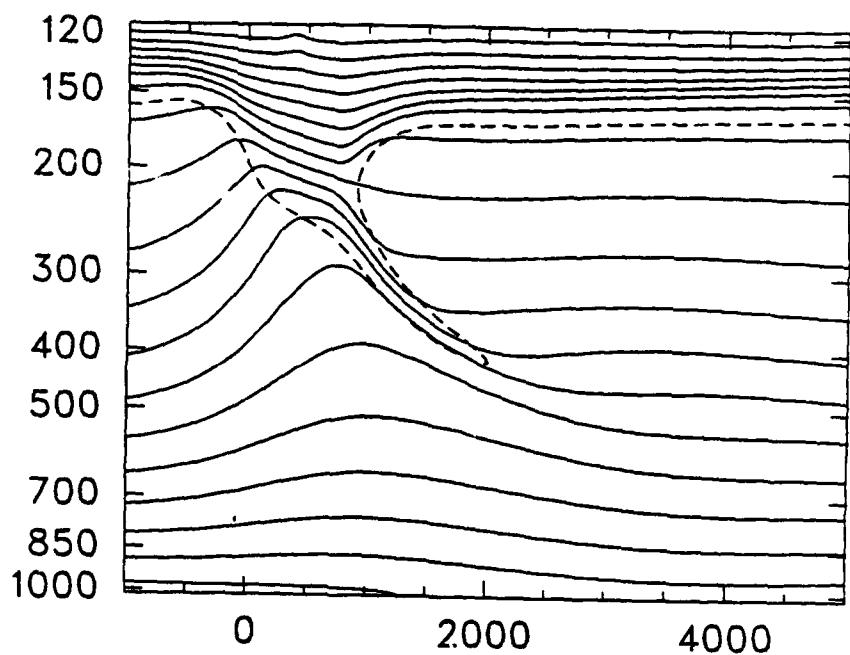
Figure 3.17: Same as fig. 3.15, except for 48 hours.
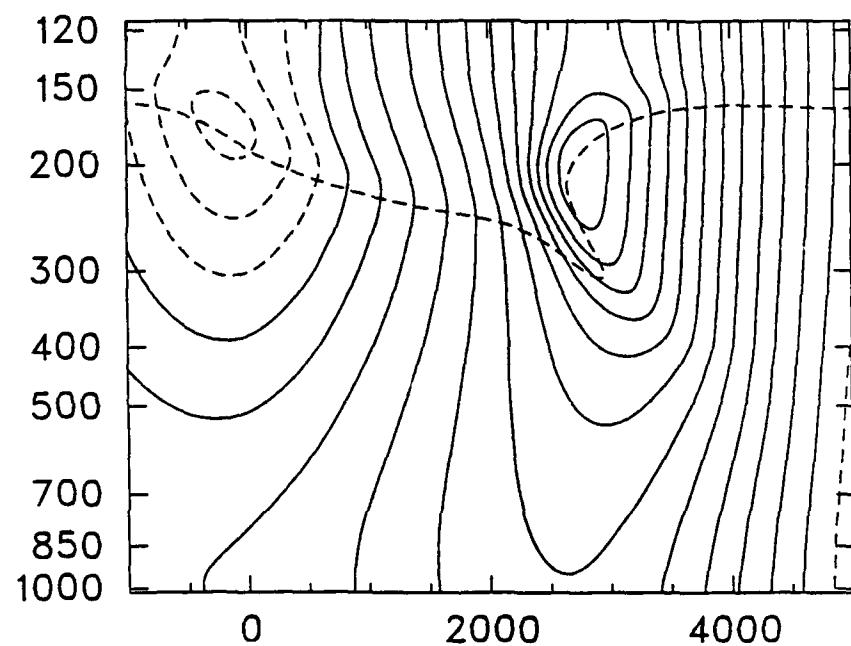
Figure 3.18: Along-front geostrophic winds at 24 hours in physical space with pressure as the vertical coordinate. Dashed line is the same as in fig. 3.15. Isotachs, drawn every 4 m/s, show the jet core above the developing fold.
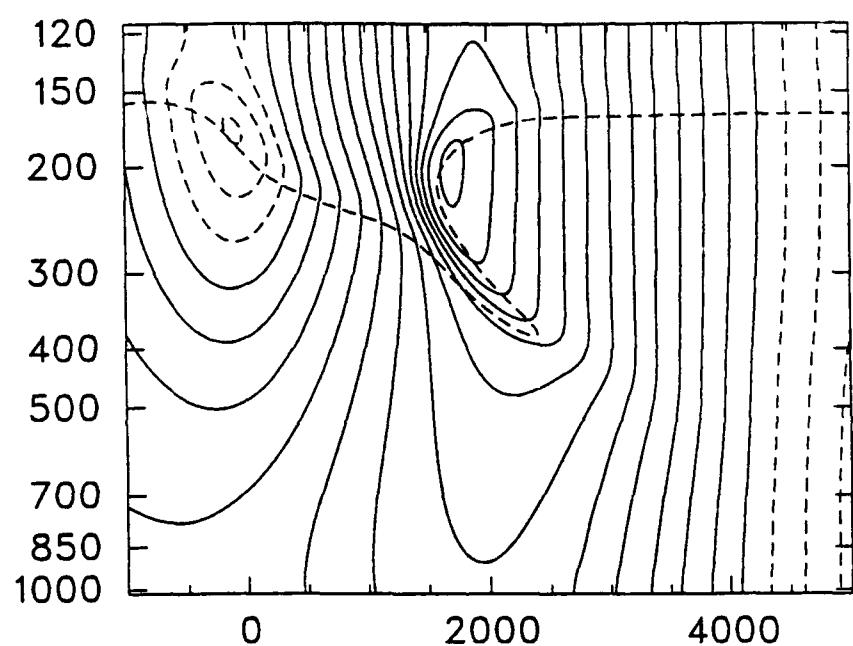
Figure 3.19: Same as fig. 3.18, except for 36 hours.
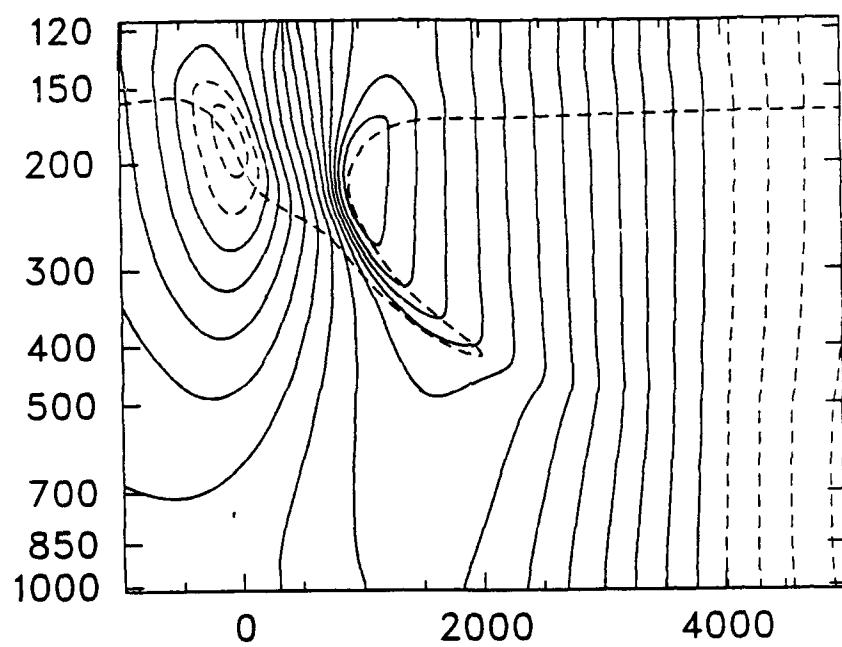
Figure 3.20: Same as fig. 3.18, except for 48 hours.
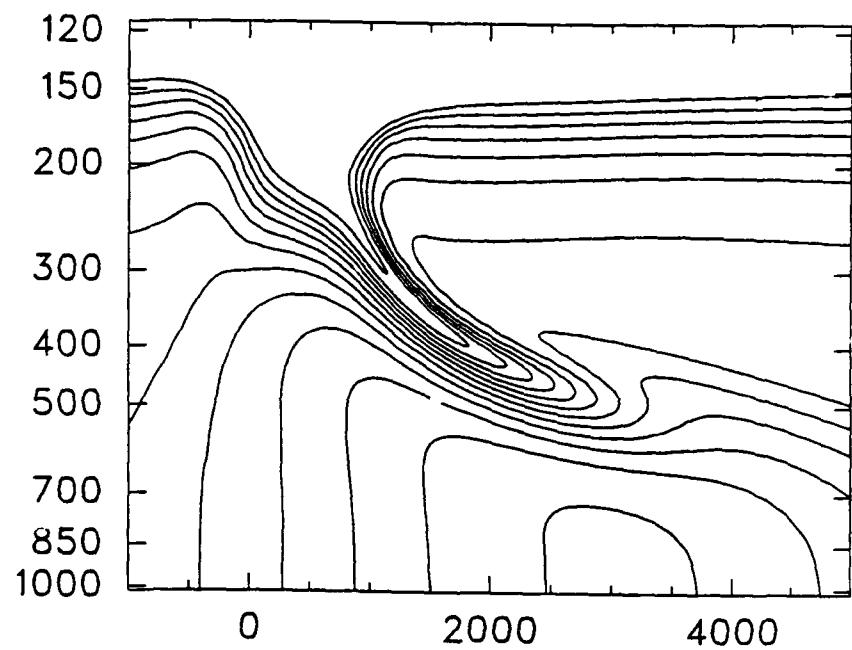
Figure 3.21: σ^* field (Pa/K) at 48 hours in physical space with pressure (mb) as the vertical coordinate. Isoline values range from 200 to 2600 as in Fig. 3.3.

Chapter 4

FRONTOGENESIS BY GENERALIZED VERTICAL WIND SHEARING

4.1 Comments

In Chapter 3 we retraced the classical frontogenesis procedure of Hoskins *et al.*. Using a generalized geostrophic deformation field which varied vertically, as well as an improved initialization of the potential vorticity field, we were able to create a realistic tropopause folding event which bears resemblance to the aforementioned observed frontal parameters. An essential feature in the success of our model is the effective shearing nature of the assumed wind field. Such an assumption is not unreasonable since significant vertical wind shearing is known to exist in baroclinic waves. Thus we can think of our deformation field as simply one example of a typical shearing environment where fronts form, and generalize our results by eliminating the deformation constraint. In its place the wind will now be specified as a function of the vertical coordinate.

Our initialization of the σ^* field in Chapter 3 allowed for the formation of surface fronts even though the lower boundary was defined as an isentropic surface. Here we examine another prescription of the initial σ^* field, with emphasis on the elimination of surface fronts so as to isolate internal processes.

4.2 Isolating Internal Processes

As an example of a more general zonal flow we set $u_g = u_g(\theta)$, and $v_g = v'_g(x, \theta, t)$ where u_g is any function of θ and v'_g is as defined in (3.2). As before we assume a straight front oriented north-south with $\partial/\partial y = 0$, and using the definitions (2.10) and our generalized geostrophic wind field, we have $\partial/\partial Y = 0$ also. Equation (2.8) reduces to

$$\frac{\partial \sigma^*}{\partial T} + u_g(\theta) \frac{\partial \sigma^*}{\partial X} = 0, \qquad (4.1)$$

which has as its solution

$$\sigma^*(X,\Theta,T) = \sigma_I^*(X - u_g T, \Theta), \qquad (4.2)$$

with σ_I^* now given by

$$\sigma_I(X,\Theta) = \sigma_T + \left\{ \frac{\tanh\left[\alpha\left(\Theta_T - \overline{\Theta}\right)\right] - \tanh\left[\alpha\left(\Theta - \overline{\Theta}\right)\right]}{\tanh\left[\alpha\left(\Theta_T - \overline{\Theta}\right)\right] - \tanh\left[\alpha\left(\Theta_B - \overline{\Theta}\right)\right]} \right\} (\sigma_B - \sigma_T)$$

$$+ \Delta\sigma \left(\frac{4\left(\Theta - \Theta_B\right)\left(\Theta_T - \Theta\right)}{\left(\Theta_T - \Theta_B\right)^2} \right)^n \tanh(\beta X), \qquad (4.3)$$

and with Θ_B and Θ_T as given in Chapter 3, $\sigma_B = 1700$ Pa/K, $\sigma_T = 100$ Pa/K, $\Delta\sigma$ half the horizontal variation of potential density in the domain, $\alpha = 1/\delta\Theta$, $\beta = 1/\delta X$, $n \geq 1$, and $\overline{\Theta}$ again a constant global average potential temperature of the tropopause. Notice that at the upper and lower boundaries (Θ_T and Θ_B), equation (4.3) reduces to the constant surfaces σ_T and σ_B. In addition, the function (4.3) has been chosen so that, when integrated, the upper and lower boundaries are also the constant pressure surfaces p_T and p_B respectively, which satisfies our original boundary assumptions in equations (2.26b) and (2.26c). The associated diagnostic equations for the interior and boundaries are unchanged from Chapter 3:

$$\frac{\partial^2 M^*}{\partial\Theta^2}\left(f^2 - \frac{\partial^2 M^*}{\partial X^2}\right) + \left(\frac{\partial^2 M^*}{\partial\Theta\partial X}\right)^2 + f^2\Gamma\sigma^* = 0, \qquad (4.4a)$$

$$\frac{\partial M^*}{\partial\Theta} = \Pi_T \quad \text{at} \quad \Theta = \Theta_T, \qquad (4.4b)$$

$$\Theta\frac{\partial M^*}{\partial\Theta} - M^* + \frac{1}{2f^2}\left(\frac{\partial M^*}{\partial X}\right)^2 = 0 \quad \text{at} \quad \Theta = \Theta_B, \qquad (4.4c)$$

and

$$M^*(\Theta,T) = M^*(\Theta,0) \quad \text{at} \quad X = -X_L, X_L. \qquad (4.4d)$$

As can be seen from (4.4d), in these experiments it was possible to narrow the domain width somewhat to a more manageable size (here we typically have $X_L = 3\lambda$). Once the zonal geostrophic winds are known or prescribed, our computational scheme is also unchanged: compute σ^* at time T; use this field to evaluate M^*; use these values in equation (2.22) to produce the wind and mass fields.

4.3 Results and Comparative Discussion

There are noteworthy differences between the experiments here and those in Chapter 3. By excluding the formation of surface fronts we isolate internal processes, but simultaneously remove possible interactions between the two through vertical motion. Several functions were considered as defining the u_g field. Examples of model runs which met with somewhat less success included a westerly jet core in the upper troposphere with wind speed decreasing both above (where they become easterly in the stratosphere) and below in a symmetric Gaussian fashion; specifically, retaining our notation from Chapter 3 we set

$$u_g = \hat{u}_g \left(\frac{\bar{\bar{\theta}} - \theta}{\delta\theta}\right) \exp\left[-\tfrac{1}{2}\left(\frac{\bar{\bar{\theta}}-\theta}{\delta\theta}\right)^2\right].$$

In these model runs no upper front was produced, but the tropopause did fold in an unrealistic fashion.

Perhaps a more realistic vertical wind distribution is given if the easterlies above the front are significantly weaker than the westerlies in the vicinity of the jet core:

$$u_g = \hat{u}_g \left[\frac{\tanh\left(\frac{\bar{\bar{\theta}}-\theta}{\theta_0}\right)}{\frac{\theta}{\bar{\bar{\theta}}-\delta\theta}}\right]^n, \tag{4.5}$$

with $\theta_0 = \delta\theta/3$, $\hat{u}_g$ a specified constant, and n any positive odd integer. Higher values of n result in a larger difference between the maximum wind speeds in the troposphere and stratosphere, respectively.

We can imagine an initial state where there is a weak horizontal gradient of σ^* corresponding to a low-amplitude upper trough. After a period of time during which the geostrophic wind field (equation 4.5) is allowed to act, a front will form due to differential advection by u_g with respect to θ-surfaces. Results using (4.5) in (4.1) are shown in figs. 4.1–4.6: 4.1–4.3 are a time sequence of the potential density field, and 4.4–4.6 are the same sequence for the thermal field with a representative tropopause value of potential vorticity.

As can be seen from these figures, the upper front as given by the σ^* field is in lesser agreement with observations than results in Chapter 3 since each individual isoline has
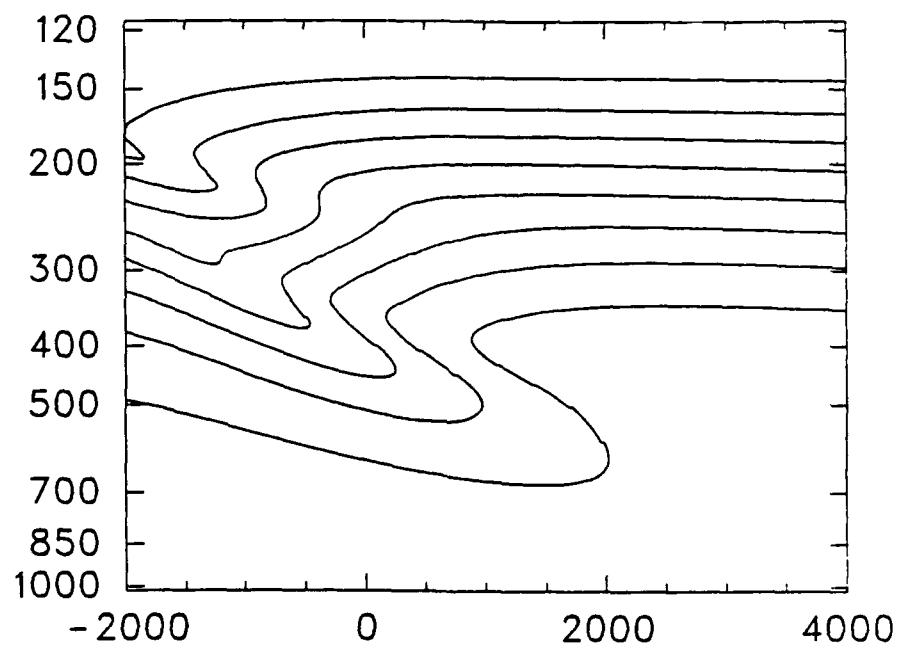
Figure 4.1: Potential density field in physical (x,p) space after u_g, as given in equation (4.5), has been allowed to act for a period of time. Isolines are every 200 Pa/K, ranging from 200 to 1600. Distance is in km on the horizontal axis.
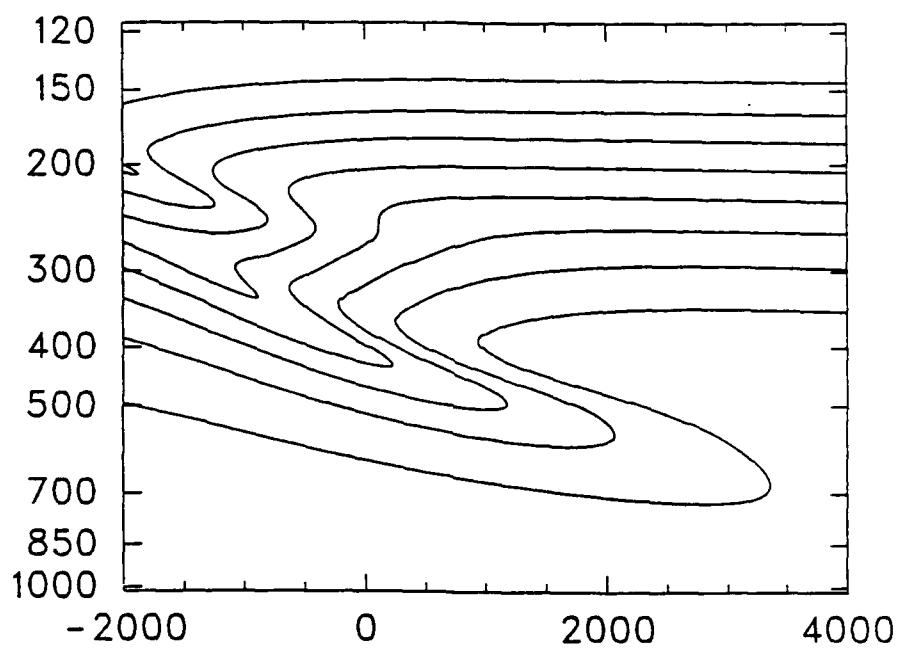
Figure 4.2: Same as fig. 4.1, except at a later time.
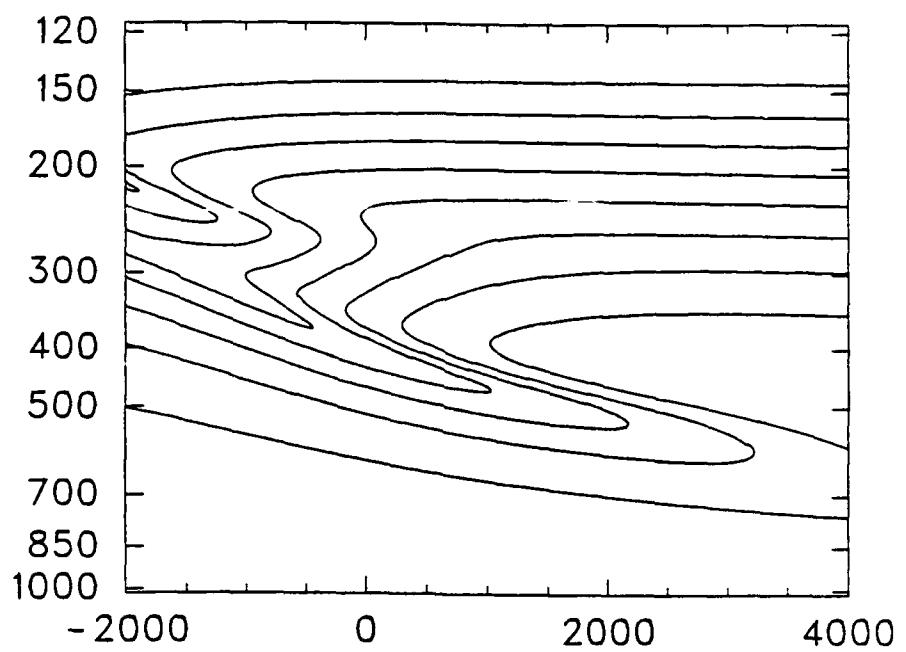
Figure 4.3: Same as fig. 4.2, except at a later time.
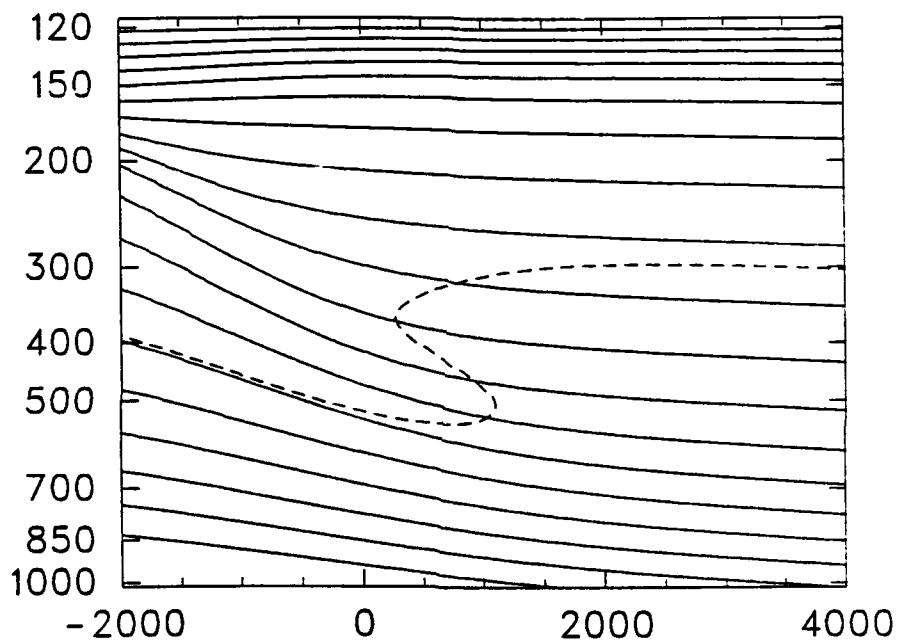
Figure 4.4: θ-field (K) and tropopause ($q = 7 \cdot 10^{-8}$ K/(Pa·s)) for the same time as fig. 4.1. Coordinate system is as in Fig. 4.1, and isentropes are every 5 K beginning with 285 K.
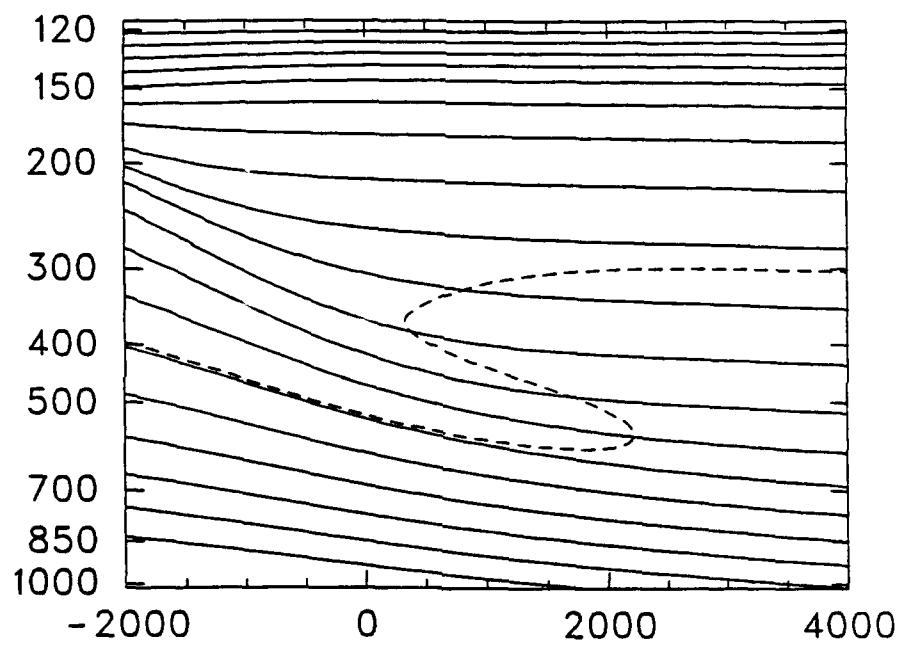
Figure 4.5: Same as fig. 4.4 but for the same time as fig. 4.2.
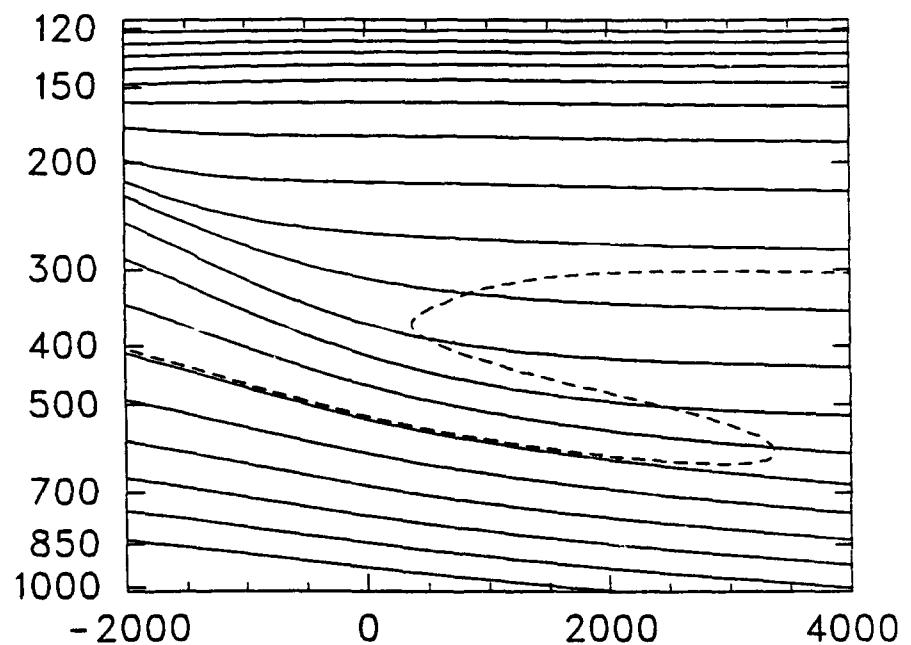
Figure 4.6: Same as fig. 4.4 but for the same time as fig. 4.3.

a relatively shallow vertical extent; that is, there is no single value of q defining a deep upper-front. Taken as a whole, however, the folding process extends deeper into the troposphere than our earlier results. The thermal field here is again in rough agreement with observations, especially with respect to its relationship with the PV field. Although the meridional wind contained realistic magnitude and shears, its proximity to the front was not well correlated. Also, the initial winds were quite strong and the jet did not develop with the developing front—these factors are attributable to the implicit relationship between our assumed σ_I^* field and the associated M^* field. As stated earlier equation (4.3) has the advantage of producing a flat PV field on the upper and lower boundaries. A drawback, however, is that this particular function would not allow a sharp vertical gradient near the tropopause while still allowing for realism in other respects, such a defining a monotonically decreasing function of θ.

Chapter 5

SUMMARY AND CONCLUSIONS

We have sought to bridge a gap in understanding the formation of internal fronts within a framework which considers them as a byproduct of baroclinic waves. Building on the accomplishments of Hoskins *et al.* by using geostrophic/isentropic coordinates with a geostrophic deformation field as a forcing mechanism, the objective of simulating tropopause folding in a balanced model much as Keyser *et al.* have done in a primitive equation model has largely been successful. We also departed from Keyser's work in that horizontal shear is neglected for our two-dimensional case; instead we considered the effects of vertical wind shears growing out of the baroclinic wave accompanied by a continuous potential vorticity field. The choice of coordinates simplifies the dynamics by implicitly including both ageostrophic and vertical motions in a system of equations which are as simple as the quasigeostrophic equations, yet are applicable in a broad and important class of motions (high relative vorticity but not highly curved flow) where quasi-geostrophic theory breaks down.

Taken as a whole our results show that internal fronts can form in a balanced two-dimensional model for two distinct cases—in the absence of a surface temperature gradient, where both surface and upper fronts can form, and when surface fronts are eliminated as a possibility—when the working definition of the tropopause is a surface of constant potential vorticity. The first case, which is covered in Chapter 3, provides the best results. With a horizontal temperature gradient of 25 K across the upper trough, the model produced a fold extending down to approximately the 500 mb level. A jet of nearly 100 kt developed along the front and above the fold with realistic wind shears when the domain was shifted from geostrophic back to physical space. Isentropic surfaces pass

through the front, showing that nearly adiabatic motions of dry stratospheric air can be advected into the mid troposphere. Thus, there is a correlation between the thermal, wind and mass fields which strongly resembles previously observed features of upper fronts. These observations used various combinations of aircraft, dropwindsonde, and rawindsonde data. The second case (Chapter 4) reinforces some results of Chapter 3: a fold/upper front results from the model, and its relationship to the potential temperature field shows similarities as well. Parameters near the front were more highly resolved, also, again due to the coordinate shift.

Based on our results there seems to be sufficient evidence to continue the study frontogenesis using a simple, two-dimensional, balanced model approach. Here we were able to simplify the dynamics of the system to essentially two equations—one predictive and one diagnostic. Due to the geostrophic momentum approximation, these equations have a more general applicability than quasigeostrophic theory. By allowing vertical wind shear to be part of the initialization process, a trough of cold air aloft bordered by warmer air on either side formed a rather deep upper front which was a result of a tropopause folding event. Unlike previous results using balanced models, reproduction of the true fold was not dependent upon the shift back to physical space—use of geostrophic coordinates simply enhanced the realism of the final product.

The introduction of more generalizations into the model leaves more areas which would benefit from further study. First it would be useful to allow isentropic surfaces to intersect the lower boundary, possibly by utilizing the positive definite scheme of Arakawa. Results would be more general and realistic of observed surface features for most cases of upper frontogenesis. Accomplishing this alone would be noteworthy by virtue of its application to other areas since the major drawback of how to handle the lower boundary condition would be solved. At the same time, the benefits of the isentropic vertical co-ordinate which have made it an increasingly popular choice, such as retention of vertical motion for the adiabatic case, would be retained. Second, more can be done to correlate observational data with our results. For example, vertical temperature profiles through a model produced fold may be similar to observations of Danielson (1980). Introducing

moisture and ozone as advected quantities should reveal a dry tropospheric layer with both anomalously high ozone values and low liquid water content at the level of the fold, indicative of the aforementioned exchange process between stratosphere and troposphere. Again, this would correlate well with observations. Third, although we included the *method* for calculating the secondary circulation across the front, recovering these fields from the model would provide insight to the tilting and subsidence effects they produce. Finally, more work can be done defining the initial fields for the Chapter 4 case (where the upper/lower boundaries are constant potential vorticity surfaces) so that there is initially a weaker geostrophic flow along the front, and the resulting jet which develops over time is better correlated with the formation of the front.

In retrospect it seems likely that the major results contained herein could also be achieved for a two-layer model. Such an application would, by virtue of its link to both previous work and current results, help in advancing the idea that much remains to be learned about the subject by employing the two-dimensional balanced approach.

REFERENCES

Andrews, D. G., 1983: A finite-amplitude Eliassen-Palm theorem in isentropic coordinates. *J. Atmos. Sci.*, **40**, 1877–1883.

Briggs, J., and W.T. Roach, 1963: Aircraft observations near jet streams. *Quart. J. Roy. Meteor. Soc.*, **89**, 225–247.

Bretherton, F. P., 1966: Critical layer instability in baroclinic flows. *Quart. J. Roy. Meteor. Soc.*, **92**, 325–334.

Buzzi, A., A. Trevisan and G. Salustri, 1981: Internal frontogenesis: A two-dimensional model in isentropic, semi-geostrophic coordinates. *Mon. Wea. Rev.*, **109**, 1053–1060.

Danielsen, E. F., 1980: Stratospheric source for unexpectedly large values of ozone measured over the Pacific Ocean during Gametag, August 1977. *J. Geophys. Res.*, **85**, 401–412.

Eliassen, A., 1948: The quasi-static equations of motion. *Geofys. Publ.*, **17**(3).

Environmental Science Services Administration, 1966: U.S. standard atmosphere supplements.

Ertel, H., 1942: Ein neuer hydrodynamischer Wirbelsatz. *Meteorologische Zeitschrift*, **59**, 277–281. An English translation of this paper and several other of Ertel's papers on potential vorticity can be obtained by writing to W. Schubert, Dept. of Atmos. Sci., Colorado State University, Fort Collins, Colorado 80523.

Fulton, S. R., 1989: Multigrid solution of the semi-geostrophic invertibility relation. *Mon. Wea. Rev.*, **117**, 2059–2066.

Haynes, P. H., and M. E. McIntyre, 1987: O. the evolution of vorticity and potential vorticity in the presence of diabatic heating and frictional or other forces. *J. Atmos. Sci.*, **44**, 828–841.

Hoskins, B.J., 1971: Atmospheric frontogenesis: some solutions. *Quart. J. Roy. Meteor. Soc.*, **97**, 139–153.

Hoskins, B.J., 1972: Non-Boussinesq effects and further development in a model of upper tropospheric frontogenesis. *Quart. J. Roy. Meteor. Soc.*, **98**, 532–541.

Hoskins, B.J., 1974: The formation of atmospheric fronts downstream in a deformation field. *J. Fluid Mech.*, **64**, *part 1*, 177–194.

Hoskins, B. J., 1975: The geostrophic momentum approximation and the semi-geostrophic equations. *J. Atmos. Sci.*, **32**, 233–242.

Hoskins, B. J., and F. P. Bretherton, 1972: Atmospheric frontogenesis models: Mathematical formulation and solution. *J. Atmos. Sci.*, **29**, 11–37.

Hoskins, B. J., and I. Draghici, 1977: The forcing of ageostrophic motion according to the semi-geostrophic equations and in an isentropic coordinate model. *J. Atmos. Sci.*, **34**, 1859–1867.

Hoskins, B. J., M. E. McIntyre and A. W. Robertson, 1985: On the use and significance of isentropic potential vorticity maps. *Quart. J. Roy. Meteor. Soc.*, **111**, 877–946.

Hoskins, B. J., and N. V. West, 1979: Baroclinic waves and frontogenesis. Part 2: uniform potential vorticity jet flows—cold and warm fronts. *J. Atmos. Sci.*, **36**, 1663–1680.

Keyser, D., and M. J. Pecnick, 1985: A two-dimensional primitive equation model of frontogenesis forced by confluence and horizontal shear. *J. Atmos. Sci.*, **42**, 1259–1282.

Keyser, D., and M. J. Pecnick, 1985: Diagnosis of ageostrophic circulations in a two-dimensional primitive equation model of frontogenesis. *J. Atmos. Sci.*, **42**, 1283–1305.

Keyser, D., and M. A. Shapiro, 1986: A review of the structure and dynamics of upper-level frontal zones. *Mon. Wea. Rev.*, **114**, 452–499.

Lorenz, E. N., 1955: Available potential energy and the maintenance of the general circulation. *Tellus*, **7**, 157–167.

McWilliams, J. C., and P. R. Gent, 1980: Intermediate models of planetary circulations in the atmosphere and ocean. *J. Atmos. Sci.*, **37**, 1657–1678.

Montgomery, R. B., 1937: A suggested method for representing gradient flow in isentropic surfaces. *Bull. Amer. Meteor. Soc.*, **18**, 210–212.

Rossby, C.-G., 1937: Isentropic analysis. *Bull. Amer. Meteor. Soc.*, **18**, 201–209.

Rossby, C.-G., 1940: Planetary flow patterns in the atmosphere. *Quart. J. Roy. Meteor. Soc.*, **66**, Suppl., 68–87.

Schubert, W. H., and B. T. Alworth, 1987: Evolution of potential vorticity in tropical cyclones. *Quart. J. Roy. Meteor. Soc.*, **113**, 147–162.

Schubert, W. H., S. R. Fulton and R. F. A. Hertenstein, 1988: Balanced atmospheric response to squall lines. *J. Atmos. Sci.*, **46**, 2478– 2483.

Shapiro, M. A., 1985: Dropwindsonde observations of an Islandic low and a Greenland mountain-lee wave. *Mon. Wea. Rev.*, **113**, 680–683.

Shapiro, M. A., T. Hampel and A. J. Krueger, 1987: The arctic tropopause fold. *Mon. Wea. Rev.*, **115**, 444–454.

Welander, P., 1955: Studies on the general development of motion in a two– dimensional, ideal fluid. *Tellus*, **7**, 141–156.

McWilliams, J. C., and P. R. Gent, 1980: Intermediate models of planetary circulations in the atmosphere and ocean. *J. Atmos. Sci.*, **37**, 1657–1678.

Montgomery, R. B., 1937: A suggested method for representing gradient flow in isentropic surfaces. *Bull. Amer. Meteor. Soc.*, **18**, 210–212.

Rossby, C.-G., 1937: Isentropic analysis. *Bull. Amer. Meteor. Soc.*, **18**, 201–209.

Rossby, C.-G., 1940: Planetary flow patterns in the atmosphere. *Quart. J. Roy. Meteor. Soc.*, **66**, Suppl., 68–87.

Schubert, W. H., and B. T. Alworth, 1987: Evolution of potential vorticity in tropical cyclones. *Quart. J. Roy. Meteor. Soc.*, **113**, 147–162.

Schubert, W. H., S. R. Fulton and R. F. A. Hertenstein, 1988: Balanced atmospheric response to squall lines. *J. Atmos. Sci.*, **46**, 2478– 2483.

Shapiro, M. A., 1985: Dropwindsonde observations of an Islandic low and a Greenland mountain-lee wave. *Mon. Wea. Rev.*, **113**, 680–683.

Shapiro, M. A., T. Hampel and A. J. Krueger, 1987: The arctic tropopause fold. *Mon. Wea. Rev.*, **115**, 444–454.

Welander, P., 1955: Studies on the general development of motion in a two– dimensional, ideal fluid. *Tellus*, **7**, 141–156.